



## PAPER

## OPEN ACCESS

## RECEIVED

5 September 2024

## REVISED

15 November 2024

## ACCEPTED FOR PUBLICATION

24 November 2024

## PUBLISHED

16 December 2024

Original Content from this work may be used under the terms of the [Creative Commons Attribution 4.0 licence](#).

Any further distribution of this work must maintain attribution to the author(s) and the title of the work, journal citation and DOI.



# Benchmarking the integration of hexagonal boron nitride crystals and thin films into graphene-based van der Waals heterostructures

Taoufiq Ouaj<sup>1</sup> , Christophe Arnold<sup>2</sup> , Jon Azpeitia<sup>3</sup> , Sunaja Baltic<sup>1</sup>, Julien Barjon<sup>2</sup> , José Cascales<sup>3</sup> , Huanyao Cun<sup>4</sup> , David Esteban<sup>3</sup> , Mar Garcia-Hernandez<sup>3</sup> , Vincent Garnier<sup>5</sup>, Subodh K Gautam<sup>2</sup>, Thomas Greber<sup>6</sup> , Said Said Hassani<sup>2</sup>, Adrian Hemmi<sup>6</sup>, Ignacio Jiménez<sup>3</sup> , Catherine Journef<sup>7</sup> , Paul Kögerler<sup>8,9</sup> , Annick Loiseau<sup>10</sup> , Camille Maestre<sup>7</sup> , Marvin Metzelaars<sup>1,8</sup> , Philipp Schmidt<sup>1</sup> , Christoph Stampfer<sup>1,11</sup> , Ingrid Stenger<sup>2</sup> , Philippe Steyer<sup>5</sup>, Takashi Taniguchi<sup>12</sup> , Bérangère Toury<sup>7</sup> , Kenji Watanabe<sup>13</sup> and Bernd Beschoten<sup>1,\*</sup>

<sup>1</sup> 2nd Institute of Physics and JARA-FIT, RWTH Aachen University, 52074 Aachen, Germany

<sup>2</sup> GEMaC, UVSQ, CNRS, Université Paris Saclay, 78035 Versailles, France

<sup>3</sup> Instituto de Ciencia de Materiales de Madrid (ICMM-CSIC), Sor Juana Inés de la Cruz 3, 28049 Madrid, Spain

<sup>4</sup> Physik-Institut, University of Zürich, 8057 Zürich, Switzerland

<sup>5</sup> INSA Lyon, Université Claude Bernard Lyon 1, CNRS, MATEIS, UMR5510, 69621 Villeurbanne, France

<sup>6</sup> Physik-Institut, University of Zürich, Zürich, Switzerland

<sup>7</sup> Université Claude Bernard Lyon 1, CNRS, LMI UMR 5615, F-69100 Villeurbanne, France

<sup>8</sup> Institute of Inorganic Chemistry, RWTH Aachen University, 52074 Aachen, Germany

<sup>9</sup> Peter Grünberg Institute (PGI-6), Forschungszentrum Jülich, 52425 Jülich, Germany

<sup>10</sup> Université Paris Saclay, ONERA, CNRS, Laboratoire d'Etude des Microstructures, 92322 Chatillon, France

<sup>11</sup> Peter Grünberg Institute (PGI-9) Forschungszentrum Jülich, 52425 Jülich, Germany

<sup>12</sup> Research Center for Materials Nanoarchitectonics, National Institute for Materials Science, 1-1 Namiki, Tsukuba 305-0044, Japan

<sup>13</sup> Research Center for Electronic and Optical Materials, National Institute for Materials Science, 1-1 Namiki, Tsukuba 305-0044, Japan

\* Author to whom any correspondence should be addressed.

E-mail: [bernd.beschoten@physik.rwth-aachen.de](mailto:bernd.beschoten@physik.rwth-aachen.de)

**Keywords:** hBN, graphene, crystal growth, thin film growth, charge carrier mobility

## Abstract

We present a benchmarking protocol that combines the characterization of boron nitride (BN) crystals and films with the evaluation of the electronic properties of graphene on these substrates. Our study includes hBN crystals grown under different conditions (atmospheric pressure high temperature, high pressure high temperature, pressure controlled furnace) and scalable BN films deposited by either chemical or physical vapor deposition (PVD). We explore the complete process from boron nitride growth, over its optical characterization by time-resolved cathodoluminescence (TRCL), to the optical and electronic characterization of graphene by Raman spectroscopy after encapsulation and Hall bar processing. Within our benchmarking protocol we achieve a homogeneous electronic performance within each Hall bar device through a fast and reproducible processing routine. We find that a free exciton lifetime of 1 ns measured on as-grown hBN crystals by TRCL is sufficient to achieve high graphene room temperature charge carrier mobilities of  $80\,000\text{ cm}^2\text{ (Vs)}^{-1}$  at a carrier density of  $|n| = 1 \times 10^{12}\text{ cm}^{-2}$ , while respective exciton lifetimes around 100 ps yield mobilities up to  $30\,000\text{ cm}^2\text{ (Vs)}^{-1}$ . For scalable PVD-grown BN films, we measure carrier mobilities exceeding  $10\,000\text{ cm}^2\text{ (Vs)}^{-1}$  which correlates with a graphene Raman 2D peak linewidth of  $22\text{ cm}^{-1}$ . Our work highlights the importance of the Raman 2D linewidth of graphene as a critical metric that effectively assesses the interface quality (i.e. surface roughness) to

the BN substrate, which directly affects the charge carrier mobility of graphene. Graphene 2D linewidth analysis is suitable for all BN substrates and is particularly advantageous when TRCL or BN Raman spectroscopy cannot be applied to specific BN materials such as amorphous or thin films. This underlines the superior role of spatially-resolved spectroscopy in the evaluation of BN crystals and films for the use of high-mobility graphene devices.

## 1. Introduction

Boron nitride (BN) with its remarkable thermal stability, chemical inertness and robust mechanical properties has long been used for various applications [1–4]. It has been demonstrated that hexagonal boron nitride (hBN) is of particular importance for applications in 2D material systems, exhibiting properties crucial for photonics and optoelectronics, such as efficient deep UV emissions [5, 6] and quantum photonics capabilities [7–10]. The high thermal conductivity [11, 12], the large electronic bandgap [5], and the ultra-flat and inert surface [13] are important prerequisites for the use as a substrate for other 2D materials or for interface engineering [14–18]. 2D materials encapsulated in hBN allow for record-breaking charge carrier mobilities in graphene [19–24], high electronic and optical quality in transition metal dichalcogenides (TMDs) [25–32] or, for example, bilayer graphene quantum devices with ultra-clean tunable bandgaps [33–36].

In fundamental research, hBN flakes exfoliated from bulk crystals grown either at high temperature and high pressure (HPHT) [37–39] or at atmospheric pressure and high temperature (APHT) [6, 24, 40–50] are employed for high-quality device fabrication due to their superior crystal quality. The synthesis of high-quality hBN crystals in a pressure-controlled furnace (PCF) is a recent development that offers new opportunities for improving material quality [51, 52]. hBN single crystals are small, a few millimeters at most, and therefore do not meet industrial manufacturing requirements. The transition of BN from the use in fundamental research to industrial applications requires process development capable of providing large area single crystal or polycrystalline films that meet both device requirements and high volume production needs.

Techniques like chemical vapor deposition (CVD) [53–58], metal-organic CVD (MOCVD) [59–62], molecular beam epitaxy (MBE) [63–66], and physical vapor deposition (PVD) [67, 68] are under development, offering potential platforms for BN substrates with sufficient interface and/or bulk qualities for the desired technological applications. Recently, amorphous (or nanocrystalline) boron nitride (aBN), has gained interest due to its ability to be grown at room temperature on arbitrary substrates [69] and its low dielectric constant [70–72]. Especially the

full encapsulation of CVD-grown graphene in direct-grown aBN was recently reported to have promising electronic properties, showing its potential as a scalable substrate for graphene and other 2D materials [71].

The evolving diversity of available BN substrates—from high-quality hBN crystals to hBN/aBN films—underlines the need for comparable and meaningful characterization methods of both the crystal quality itself and the ability to be used as substrate in van der Waals heterostructures. To assess the crystal quality, BN is mostly investigated by cathodoluminescence (CL) [73–75], photoluminescence (PL) [64, 76, 77] or Raman spectroscopy [2, 78, 79]. Raman spectroscopy gives a rapid and non-invasive way to extract the quality of BN films and therefore is an indispensable tool to efficiently monitor the parameter tuning during optimization of growth processes. On the other side, CL measurements and especially time-resolved cathodoluminescence (TRCL) measurements yield a much more sensitive way to evaluate the crystal quality and to gain a deeper understanding of the type of crystal defects [73–75]. Here, the free exciton lifetime, which is limited by exciton-defect scattering, yields a sensitive benchmark for the bulk crystal quality. However, CL measurements are not suitable for most scalable BN growth approaches as they are only applicable to crystalline and thick ( $>10\mu\text{m}$ ) hBN. While these evaluations are highly important for benchmarking the quality of hBN crystals for optical applications with hBN as the active layer, methods to evaluate the surface quality become equally important when used as a substrate [80]. For example, correlations between the amount or type of defects and the surface roughness seem possible but remain a topic under investigation [81].

Graphene, due to its exceptional high charge carrier mobility, is one of the most interesting 2D materials to be used in combination with BN. Additionally to the interest due to its electronic properties, graphene is highly sensitive to charge disorder and surface roughness of the substrate, drastically limiting the device performance [20, 82]. Due to both, its huge potential for future high-mobility applications and its high sensitivity to the underlying substrate, the evaluation of graphene itself on the substrate of interest is an appealing way to investigate the suitability of various BN films or crystals as a

substrate for 2D materials. Spatially-resolved confocal Raman microscopy on graphene encapsulated in BN provides a very powerful and sensitive way to directly assess strain, doping, and nm-strain variations [80, 83–85] and directly link it to the electronic properties extracted from charge transport measurements on Hall bar devices [22–24, 82].

Here, we present a comprehensive evaluation of various BN substrates and present a benchmarking protocol covering the characterization of the BN as well as the evaluation of the electronic properties of exfoliated graphene on these BN substrates. Our study includes the growth of both high-quality hBN crystals grown via APHT or in a PCF and the growth of scalable BN films via PVD or CVD (section 2). We extract the free exciton lifetime from TRCL measurements to compare the crystal quality of BN crystals and evaluate both exfoliated flakes and films via Raman spectroscopy (section 3). Using exfoliated graphene, we fabricated dry-transferred devices on the BN substrates to assess the interface quality via spatially-resolved Raman spectroscopy (section 4). To establish reliable benchmarks we focus on the full width at half maximum (FWHM) of the graphene Raman 2D peak, which we identify as the most sensitive benchmark for an early-stage evaluation of the suitability for a diverse set of BN substrates (section 5). Following a newly developed fabrication scheme, with a focus on rapid processing, we build Hall bar structures (section 6) to extract the charge carrier mobility at different charge carrier densities (section 7). We demonstrate that graphene encapsulated in APHT hBN crystals compares in electronic quality to graphene encapsulated in HPHT-grown hBN crystals, reaching room temperature charge carrier mobilities around  $80\,000\text{ cm}^2(\text{Vs})^{-1}$  at a charge carrier density of  $n = 1 \times 10^{12}\text{ cm}^{-2}$ . Importantly, we identify a free exciton lifetime of above 1 ns to be sufficient to achieve these high charge carrier mobilities and of 100 ps for charge carrier mobilities up to  $30\,000\text{ cm}^2(\text{Vs})^{-1}$ . Specifically, we demonstrate that graphene on PVD-grown nanocrystalline boron nitride with a graphene 2D peak FWHM below  $22\text{ cm}^{-1}$  consistently yields charge carrier mobilities exceeding  $10\,000\text{ cm}^2(\text{Vs})^{-1}$ . This underscores the potential of PVD-grown BN films as scalable substrates for high-mobility graphene devices.

## 2. Growth and preparation of boron nitride

In figure 1 the growth and preparation conditions of hBN crystals (APHT and PCF growth) and of BN thin films (PVD and CVD growth) are summarized.

### 2.1. Atmospheric pressure and high temperature (APHT)

The hBN crystals in this study were grown from an iron flux (at RWTH) or chromium-nickel (at RWTH and GEMaC) flux via the APHT method (see reference [24] for details on the growth at RWTH). A schematic illustration of the growth setup is shown in figure 1(a). The boron source is either boron powder (RWTH) mixed with the metal pieces or a pyrolytic BN crucible (GEMaC). The system is first annealed at high temperature under a continuous gas flow of either  $\text{H}_2$  and Ar (RWTH) or  $\text{N}_2$  (GEMaC) to minimize contaminations with oxygen and carbon. The hBN crystal growth is started upon introduction of  $\text{N}_2$  while maintaining a constant pressure. After a soaking phase at high temperature to saturate the metal flux with B and N, the furnace is cooled down to a lower temperature at a slow rate (typically between  $0.5\text{ }^\circ\text{C/h}$  and  $4\text{ }^\circ\text{C/h}$ ). The system is then quickly quenched down to room temperature. The resulting thick hBN crystal layer is firmly attached to the underlying metal ingot, as seen in figure 1(a) (right upper panel). The hBN crystal sheet can be detached from the metal ingot by immersion in hydrochloric acid at room temperature, see the detached crystal sheet in the lower right panel of figure 1(a). This step does not affect the quality of the hBN crystals and simplifies the further processing of the hBN crystals for exfoliation and subsequent dry-transfer [24].

### 2.2. Growth in a pressure-controlled furnace (PCF)

In the PCF method, hBN crystals are grown from the liquid phase of  $\text{Li}_3\text{BN}_2 - \text{BN}$  at high temperature [52, 86, 87]. The  $\text{Li}_3\text{BN}_2$  powder is pre-synthesized from  $\text{Li}_3\text{N}$  (Sigma Aldrich, purity  $> 99.5\%$ ) [88] and mixed with commercial hBN powder (20 wt% hBN and 80 wt%  $\text{Li}_3\text{BN}_2$ ) in a molybdenum crucible. Since  $\text{Li}_3\text{BN}_2$  is very sensitive to air and moisture, the growth preparation is performed under inert conditions and careful handling is necessary throughout the whole process. Both, hBN powder and crucibles are pre-treated at  $1200\text{ }^\circ\text{C}$  under vacuum and an Ar/ $\text{H}_2$  gas mix to remove potential contaminations. The growth is performed in a pressure-controlled furnace (PCF) [51, 52] (schematically shown in figure 1(b)) during a fast cooling after a dwelling time of 2 h at  $1800\text{ }^\circ\text{C}$  and a pressure of 180 MPa under Ar atmosphere. The temperature and the pressure are increased at a rate of  $100\text{ }^\circ\text{C min}^{-1}$  and  $10\text{ MPa min}^{-1}$ . The chamber is initially purged three times (Ar filling followed by pumping) to remove oxygen and moisture. The sample obtained is an ingot composed of hBN crystals embedded in a solidified  $\text{Li}_3\text{BN}_2$  matrix.  $\text{Li}_3\text{BN}_2$  dissolution is then performed to retrieve individual crystals. They show a lateral size

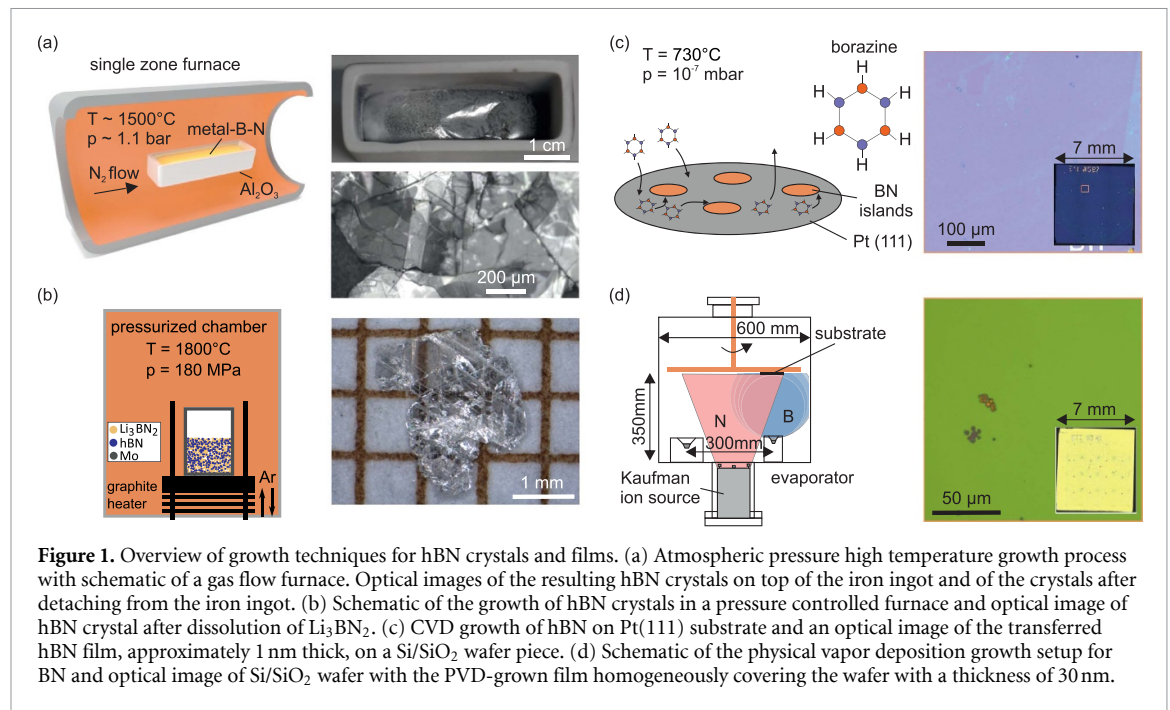


**Figure 1.** Overview of growth techniques for hBN crystals and films. (a) Atmospheric pressure high temperature growth process with schematic of a gas flow furnace. Optical images of the resulting hBN crystals on top of the iron ingot and of the crystals after detaching from the iron ingot. (b) Schematic of the growth of hBN crystals in a pressure controlled furnace and optical image of hBN crystal after dissolution of  $\text{Li}_3\text{BN}_2$ . (c) CVD growth of hBN on Pt(111) substrate and an optical image of the transferred hBN film, approximately 1 nm thick, on a Si/SiO<sub>2</sub> wafer piece. (d) Schematic of the physical vapor deposition growth setup for BN and optical image of Si/SiO<sub>2</sub> wafer with the PVD-grown film homogeneously covering the wafer with a thickness of 30 nm.

ranging from several hundreds of micrometers to few millimeters, exemplary shown in figure 1(b), in the right image. The crystals have been previously used as encapsulants for TMDs and graphene to obtain optical and electronic devices [52, 89].

### 2.3. Chemical vapor deposition (CVD)

For the growth of hBN layers, Pt(111) thin films with a thickness of 500 nm were prepared on sapphire wafers [90]. The hBN films were grown via CVD in an ultra-high vacuum cold-wall chamber for wafers up to 4-inch [91, 92]. Prior to all hBN preparations, the Pt/sapphire substrates were cleaned by a series of argon sputtering, O<sub>2</sub> exposure and annealing cycles to 1200 K until sharp Pt(111) ( $1 \times 1$ ) LEED patterns were observed. Subsequently, hBN layers were prepared at temperatures above 1000 K with borazine ( $\text{HBNH}$ )<sub>3</sub> as precursor with a partial pressure of  $10^{-7}$  mbar (figure 1(c)). The quality of grown hBN layers were evaluated with scanning low energy electron diffraction (x-y LEED), x-ray photoelectron spectroscopy (XPS), ultraviolet photoelectron spectroscopy (UPS), scanning tunneling microscopy (STM) and atomic force microscopy (AFM). The reported thickness is derived from XPS intensity values.

The transfer procedure employs the electrochemical ‘bubbling’ method [93]. First, the hBN/Pt(111) sample was spin-coated with 4 wt% polymethyl methacrylate (PMMA) (495 K). Then we put the PMMA/hBN/Pt sample as working electrode and a Pt wire as counter electrode in a 1.0 M KCl solution. A negative voltage between  $-3$  V and  $-5$  V was applied

to the sample to delaminate the hBN/PMMA film from the substrate. The delaminated hBN/PMMA film was then rinsed in ultrapure water (Milli-Q Advantage A10) and transferred onto a clean 280 nm Si/SiO<sub>2</sub> substrate with gold markers. In the next step, the PMMA was removed via a sequence of acetone/ethanol baths and gradual annealing in air at temperatures up to 600 K for 3 h. Figure 1(c) shows a representative transferred hBN film with a thickness of approximately 1 nm.

### 2.4. Physical vapor deposition (PVD)

Thin nanocrystalline BN films are grown via physical vapor deposition using an ion beam assisted deposition process (IBAD-PVD). The films exhibit hexagonal bonding structure, as assessed by x-ray absorption near edge spectroscopy (XANES) [94, 95] but lack of x-ray diffraction. The films were grown directly on Si/SiO<sub>2</sub> wafers with an oxide thickness of 285 nm and pre-defined Cr/Au marker. The growth was performed at room temperature using nitrogen gas and a solid boron source. The IBAD process consisted in the interaction of a directional beam of 500 eV nitrogen ions from a Kaufman source, with concurrent boron atoms from an electron beam evaporator. The growth setup is schematically depicted in figure 1(d). The N-ion and B-atom fluxes were carefully tuned to obtain stoichiometric BN and avoid other  $\text{B}_x\text{N}_y$  phased and bonding configurations [67]. The thickness of the resulting BN film is 30 nm and homogeneously covers the whole wafer, as shown in figure 1(d).



### 3. Cathodoluminescence and Raman spectroscopy on BN crystals and films

The as-grown hBN crystals (APHT and PCF) are examined by means of TRCL measurements and spatially-resolved confocal Raman microscopy. Raman spectroscopy offers a fast and non-invasive tool to spatially probe optical phonons and their lifetimes, which provide a measure of the crystallinity of hBN [2]. Time-resolved cathodoluminescence (TRCL) measurements allow to determine the lifetimes of the free excitons, which are strongly affected by scattering with defects, providing a valuable and sensitive tool to locally probe the crystal quality of hBN crystals.

#### 3.1. Cathodoluminescence

TRCL measurements were performed on isolated bulk hBN crystals. For each supplier (GEMaC, RWTH, LMI), crystals from multiple growth batches were investigated. The deep UV spectra were recorded at room temperature in a JEOL7001F field-emission-gun scanning electron microscope (SEM) coupled to a Horiba Jobin-Yvon cathodoluminescence (CL) detection system, as described in detail in earlier works [73–75]. To allow for time resolution, a custom-built fast-beam blaster was installed inside the SEM column, as described in [75]. The dynamics of the free exciton population is captured by measuring the time-dependent CL intensity in a wavelength range of  $215 \pm 7.5$  nm with a temporal resolution of 100 ps. This spectral range corresponds to the main luminescence feature of high quality hBN crystals. The 215 nm CL signal results from the indirect exciton recombination assisted via optical phonons. To focus on bulk properties and minimize surface recombinations, the electron beam acceleration voltage was set to 15 kV [73, 96]. The current was maintained at a low value of 85 pA to prevent nonlinear effects [97]. An exemplary TRCL measurement for each type of hBN crystal investigated is shown in figure 2. At  $t = 0$ , the luminescence peak intensity is normalized to 1, to allow for better comparison of the time evolution. The free exciton lifetime  $\tau_{CL}$  is extracted by fitting the first decay with a single exponential decay function [75]. We obtain  $\tau = 0.15$  ns, 1.67 ns and 3.32 ns for PCF (LMI), APHT (RWTH) and APHT (GEMaC) crystals, respectively. Statistical evaluation (mean and standard deviation) across different growth batches and spatial positions on the crystals yielded  $\tau = (0.11 \pm 0.07)$  ns,  $(1.4 \pm 0.3)$  ns and  $(3.0 \pm 0.4)$  ns for 22, 13 and 8 measured areas on PCF (LMI), APHT (RWTH) and APHT (GEMaC), respectively. We emphasize the need for statistical evaluation due to notable crystal-to-crystal variations.

The variation in free exciton lifetimes is associated with differences in defect densities in the crystals.

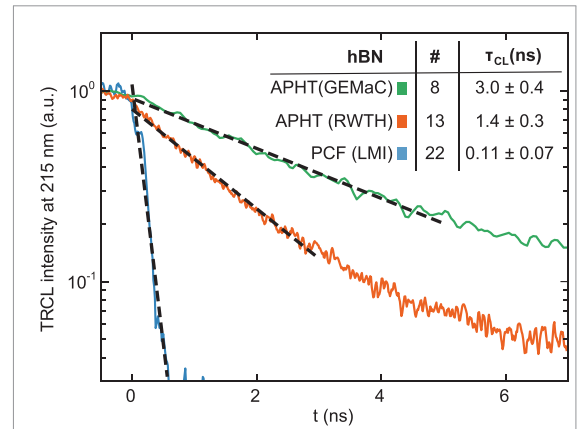
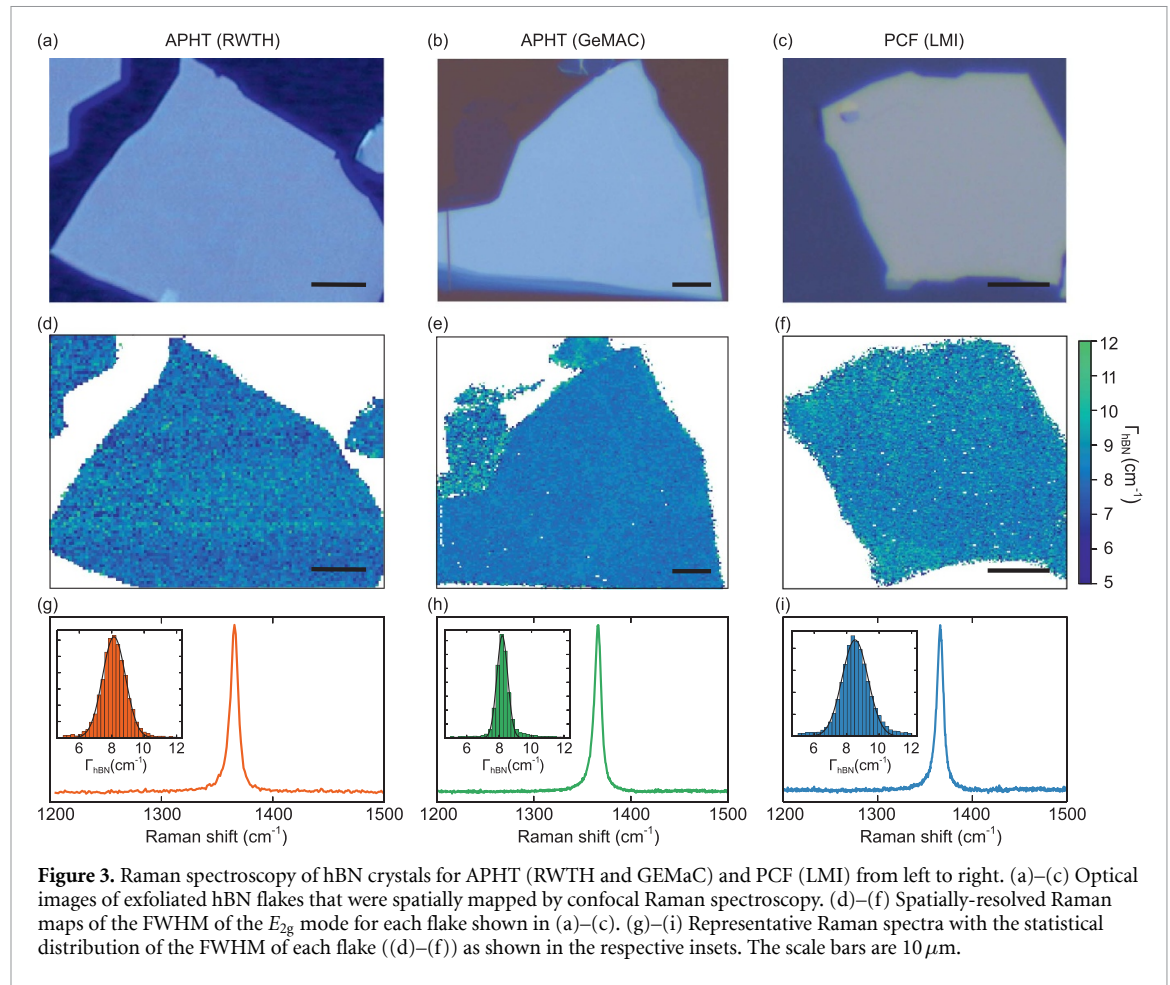


**Figure 2.** Decay of the free exciton luminescence at 215 nm for hBN crystals grown by APHT (RWTH and GEMaC) and PCF (LMI) measured by time-resolved cathodoluminescence. The luminescence intensity is normalized to 1 at  $t = 0$  for all measurements. A representative trace is shown for each crystal type together with an exponential fit to extract the respective lifetime  $\tau_{CL}$ . The table in the inset shows the averaged lifetimes from measurements at different crystal positions and batches with the total number of measurements.

We note that APHT-grown crystals exhibit lifetimes similar to those produced via the HPHT method [75] which is consistent with a low defect density. In contrast, PCF-grown crystals show significantly shorter lifetimes. The higher defect density could result from vacancies, impurities, or structural anomalies, which all may affect the free lifetime. The variations in lifetimes, even within crystals grown by the same method, highlights the need for careful crystal selection for specific experiments or applications. Understanding these defect-induced changes in the optical properties is crucial for the further development of hBN applications in optoelectronics and quantum technology. The benchmarking of hBN crystals via TRCL also sets the stage for understanding their role as substrates in graphene-based devices. The observed variation in the exciton lifetime of hBN grown by the different methods is expected to correlate with the electronic quality of encapsulated 2D materials. Its impact on the charge carrier mobility in hBN/graphene/hBN Hall bar devices will be detailed further below.

#### 3.2. Confocal Raman spectroscopy

Raman spectroscopy is a practical and widely used optical probe for characterizing both hBN crystals and thin films. Its advantage of accessibility makes it an important tool for monitoring the effect of changes in the growth parameters on the crystal quality of BN. The primary benchmark for assessing the crystal quality of hBN via Raman spectroscopy is the FWHM  $\Gamma_{E_{2g}}$  of the  $E_{2g}$  Raman peak, which correlates with the lifetime  $\tau_{E_{2g}}$  of optical phonons corresponding to intralayer vibrations of B and N atoms [98]. The



contributions to the phonon linewidth in hBN with a natural isotopic content of boron originate primarily from isotopic disorder-induced scattering, anharmonic phonon decay, or impurity scattering [99]. Thus, in hBN with the same crystal structure and isotope distribution, the variations in FWHM are mainly due to the degree of disorder in the crystal [2]. Changes in bond lengths due to increased defect density or not-purely  $\text{sp}^2$ -hybridized bonds might also impact the FWHM, as these factors contribute to averaging effects over phonons of different frequencies. Typically, high quality hBN crystals grown via HPHT or APHT exhibit a FWHM around  $8\ \text{cm}^{-1}$  [2, 79, 100]. For thin BN films this value can increase up to  $40\ \text{cm}^{-1}$  [2].

### 3.2.1. Experimental setup

Raman measurements were conducted using a commercial confocal micro-Raman setup (WITec alpha 300 R) at room temperature. We utilized a  $532\ \text{nm}$  excitation wavelength, a laser power of  $2\ \text{mW}$  and a  $100\times$  magnification objective with a numerical aperture of  $0.9$ . The inelastically scattered light was collected through a fibre (core diameter  $100\ \mu\text{m}$ ) and sent to a CCD through a half meter spectrometer equipped with a  $1200\ \text{lines mm}^{-1}$  grating. For

linewidth analysis of high-quality hBN crystals, we employed a grating with  $2400\ \text{lines mm}^{-1}$ .

### 3.2.2. hBN crystals

We start by exfoliating thin hBN flakes from the bulk crystals using tape (Ultron 1007 R) onto  $\text{Si/SiO}_2$  wafer with a  $90\ \text{nm}$  oxide layer and observe similar distribution of thicknesses and lateral sizes for flakes from all crystal suppliers. Flakes with thicknesses between  $20\ \text{nm}$  and  $40\ \text{nm}$  were selected based on their color contrast towards the substrate [101], as these thicknesses are optimal for building state-of-the-art hBN-encapsulated graphene devices. In figures 3(a)–(c), we present optical images of representative flakes from the three suppliers ((a) for APHT (RWTH), (b) for APHT (GeMaC), and (c) for PCF (LMI)). All flakes look similar in terms of contamination or thickness homogeneity. This is inferred from the optical images in figures 3(a)–(c), where each crystal flake shows a single homogenous optical contrast to the substrate and no optically visible contaminations.

The FWHM of the  $E_{2g}$  peak is extracted by fitting a single Lorentzian function to the individual Raman spectra. Spatially-resolved maps of the FWHM are shown in figures 3(d)–(f). A respective single Raman

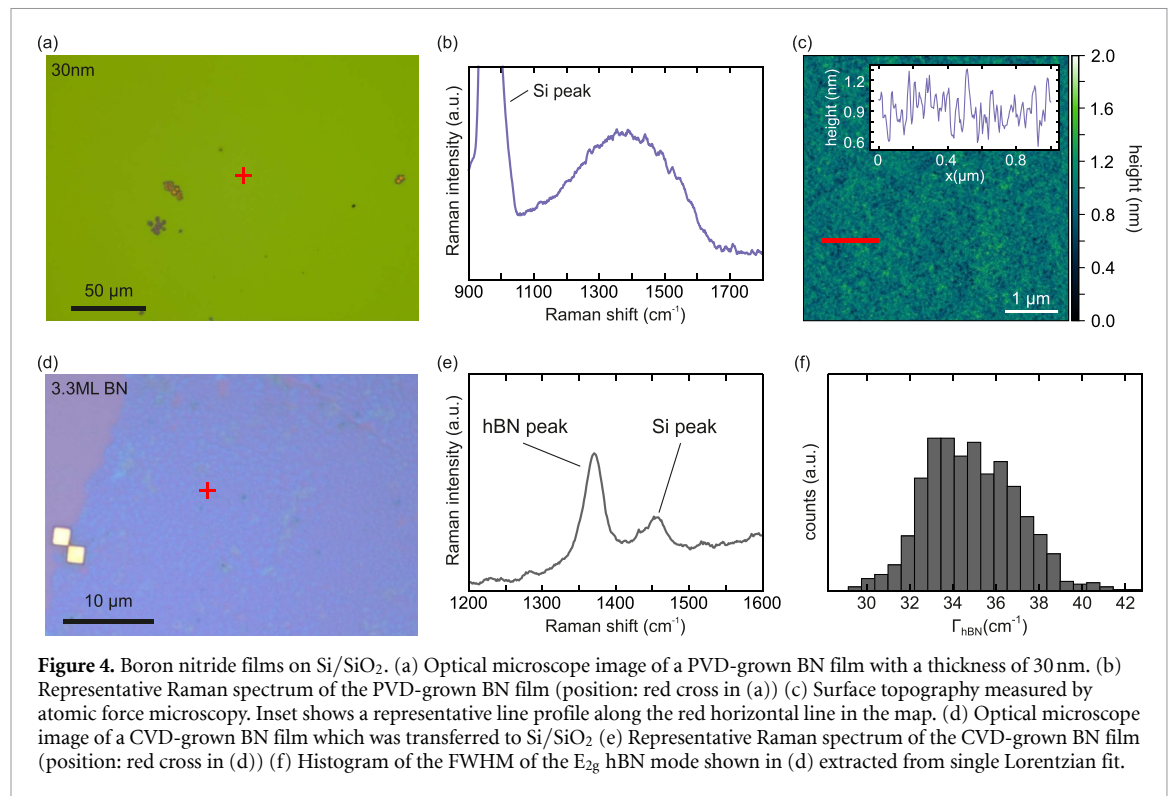


**Figure 4.** Boron nitride films on Si/SiO<sub>2</sub>. (a) Optical microscope image of a PVD-grown BN film with a thickness of 30 nm. (b) Representative Raman spectrum of the PVD-grown BN film (position: red cross in (a)) (c) Surface topography measured by atomic force microscopy. Inset shows a representative line profile along the red horizontal line in the map. (d) Optical microscope image of a CVD-grown BN film which was transferred to Si/SiO<sub>2</sub> (e) Representative Raman spectrum of the CVD-grown BN film (position: red cross in (d)) (f) Histogram of the FWHM of the  $E_{2g}$  hBN mode shown in (d) extracted from single Lorentzian fit.

spectrum at a representative position, along with the corresponding histogram to the FWHM map, are shown in figures 3(g)–(i).

There is a narrow hBN Raman peak around  $1365\text{ cm}^{-1}$  for all flakes. The maps in figures 3(d)–(f) reveal a homogenous and narrow distribution of the FWHM, suggesting uniform crystal quality throughout the exfoliated flakes. A closer inspection of the statistical distribution (insets of (g)–(i)), reveals a Gaussian distribution of the FWHM around  $8\text{ cm}^{-1}$ , demonstrating high crystallinity for all flakes. These values are comparable to previous studies on APHT or HPHT grown hBN [2]. Interestingly, we observe no significant difference in the Raman FWHM between PCF and APHT crystals. This observation seems surprising since the CL lifetime of the PCF-grown hBN flakes is more than an order of magnitude shorter than the respective lifetimes of the APHT-grown hBN crystals (see figure 2). It is, however, important to emphasize again that main contributions to the  $E_{2g}$  peak's FWHM in natural hBN results from isotopic disorder [99], that is typically the same for all. While isotopic disorder is generally the same for all hBN crystals, variations in defect type and density can significantly vary between different growth methods. Our studies suggest that the presence of crystal defects in high-quality hBN crystals can barely be probed by Raman spectroscopy. Analyzing the lifetimes of free excitons, on the other hand, offers a significantly more sensitive tool for the local probing of crystal defects.

### 3.2.3. BN films

We next evaluate boron nitride films, which are either grown directly on the Si/SiO<sub>2</sub> substrate (PVD) or grown by means of CVD and then wet-transferred to a Si/SiO<sub>2</sub> substrate. In the case of boron nitride films, cathodoluminescence measurements are not feasible, mainly due to the small thickness of the films. An optical image of the PVD-grown film is shown in figure 4(a). We observe a homogeneously grown film over the entire wafer with some spots where the BN is damaged. In figure 4(b) we additionally show a Raman spectrum at a representative position. In contrast to the previously shown Raman spectra of flakes from exfoliated hBN crystals, we do not observe a single narrow Raman peak. Instead, a broad response ranging from  $1100\text{ cm}^{-1}$  to  $1600\text{ cm}^{-1}$  is observed. This can be related to the amorphous nature of the BN film, which leads to a strong broadening of the Raman peak due to the inclusion of nanocrystalline regions within the BN film [102]. The broadening may also result from random strain effects [71]. They lead to an averaging of different bond lengths between the atoms resulting in a statistical averaging of the Raman response due to variations in the phonon frequencies.

As the PVD grown BN films will later be used as a substrate for graphene, we next explore their surface roughness by atomic force microscopy (AFM). Figure 4(c) displays an AFM image for a small region of the sample shown in figure 4(a). A root mean square (RMS) roughness of  $0.2\text{ nm}$  is extracted from this map. This low value is in line with RMS values

of hBN and the 2D semiconductor WSe<sub>2</sub>, which have proven to be ideal substrates for graphene [80].

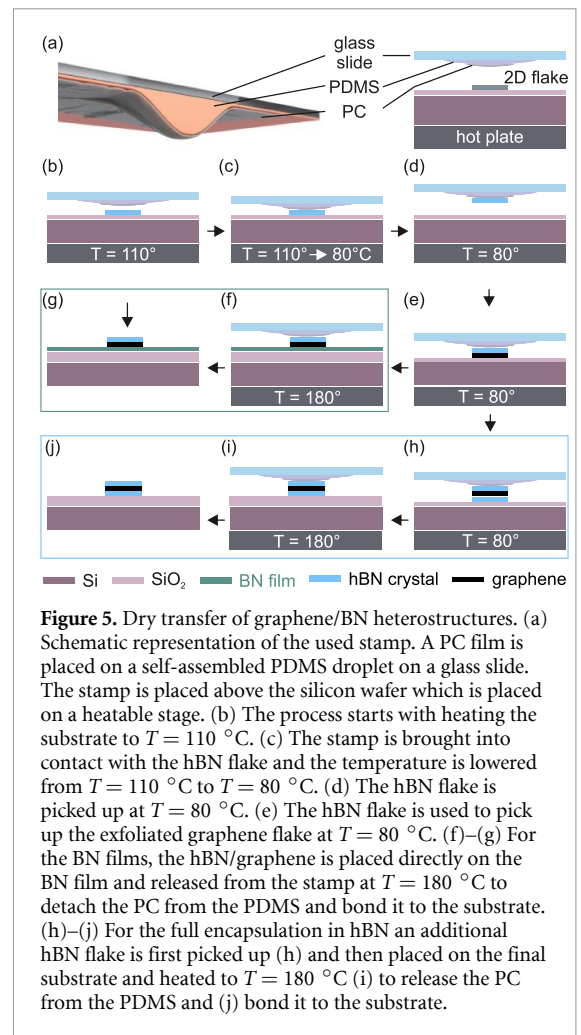
In figure 4(d) we show an optical image of the CVD grown BN film which was transferred on SiO<sub>2</sub>. Due to the wet-transfer process and because multiple layers of hBN are transferred on top of each other, the BN film does not have a homogenous thickness. From XPS measurements we estimate an average thickness of 3 layers of hBN. The Raman spectrum at a representative position is shown in figure 4(e) together with a histogram of the distribution of the FWHM in panel (f). We observe a well-defined hBN Raman peak at  $\omega_{E_{2g}} = 1365 \text{ cm}^{-1}$  with a FWHM of  $\Gamma_{E_{2g}} = 34 \text{ cm}^{-1}$ . The large FWHM is in striking contrast to the previously discussed crystals but comparable to other BN films shown in literature [103–105]. We attribute the large FWHM to the wet transfer procedure and the remaining PMMA residues on the transferred BN film.

To conclude the pre-characterization of BN crystals and films, we note that there is no common method which is either sensitive enough or applicable to all forms of BN, i.e. crystals and films. Especially, for nanocrystalline or amorphous BN films, which are recognized as potential substrates for scaled devices, the usual characterization methods are not feasible. We therefore proceed with the evaluation of graphene in contact with BN, by using graphene as a sensitive detector for the suitability of the underlying BN/hBN substrate for charge transport.

#### 4. Dry-transfer of graphene encapsulated in BN

The next step in the benchmarking protocol is to build van der Waals heterostructures using BN material to fully encapsulate graphene. The substrate quality of BN is then explored by probing the electronic properties of graphene using both spatially-resolved Raman spectroscopy and charge transport measurements.

For the stacking of the heterostructures we start by exfoliating hBN and graphene flakes onto 90 nm Si/SiO<sub>2</sub>. The flakes are searched and classified using a home-built automatic flake detection tool [101]. Suitable flakes with a thickness between 20 and 40 nm are identified and stacked on top of each other using standard dry-transfer methods with poly(bisphenol A carbonate) (PC) film on top of a drop-shaped polydimethylsiloxane (PDMS) stamping tool [106]. The stacking process is schematically depicted in figure 5. For the benchmarking of hBN crystals (APHT and PCF), graphene is picked up using hBN flakes, which were exfoliated from their respective bulk crystals while for the evaluation of BN films the graphene is picked up by exfoliated HPHT-grown hBN (figures 5(b)–(d)). In the next step, the



hBN/graphene half stack is either transferred onto corresponding hBN crystal flakes (figures 5(h)–(j)) or placed onto the BN films (figures 5(f)–(g)). The protection of graphene from the top by an hBN crystal is important to ensure heterostructures of comparable quality and exclude influences on the graphene quality and device performance that can be caused by chemicals or airborne contaminations [107] during the subsequent processing steps. Optical microscope images of the finished stacks are shown in figures 7(a)–(e). The lateral size of the stacks is limited by the size of the exfoliated hBN and graphene flakes. Within this project, we characterized in total over 40 dry-transferred samples to obtain a statistical evaluation of the various BN substrate and to exclude sample-to-sample variations.

#### 5. Raman spectroscopy on BN-graphene heterostructures

##### 5.1. Extraction of strain, strain variations and doping

We first give an overview on the key concepts of graphene-based Raman spectroscopy. Figure 6(a)



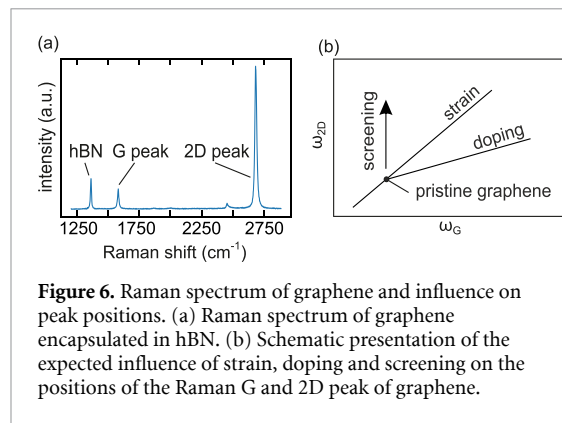


**Figure 6.** Raman spectrum of graphene and influence on peak positions. (a) Raman spectrum of graphene encapsulated in hBN. (b) Schematic presentation of the expected influence of strain, doping and screening on the positions of the Raman G and 2D peak of graphene.

shows a typical Raman spectrum of graphene encapsulated in hBN crystals. Three prominent peaks are typically observed corresponding to the above analyzed hBN  $E_{2g}$  peak and the graphene G and 2D peak. The G peak in graphene results from out-of-phase in-plane vibrations of two carbon atoms of the two sublattices and involves phonons from the  $\Gamma$ -point, whereas the double resonant 2D peak corresponds to a breathing mode, involving phonons near the K-point [108–110].

A crucial and sensitive quantity for the evaluation of the electronic properties of graphene is the FWHM of the 2D peak, which is directly connected to the extent of nm-scale strain variations within the laser spot [84] and therefore also contains information on the roughness of the substrate [80]. As strain variations locally break the hexagonal symmetry of the lattice, a vector potential is induced which in turn leads to an increased probability of backscattering of electrons in charge transport leading to a reduced charge carrier mobility [82]. The 2D FWHM is therefore the main quantity of interest in our study as it directly connects the interface quality given by the BN with the electronic quality of the adjacent graphene sheet.

The G and 2D peak are both susceptible to strain as well as doping [83] and the 2D peak position is additionally influenced by dielectric screening from the environment [111], which is, however, not relevant in the scope of this study. To separate the effects of strain and doping from spatially-resolved Raman maps, the positions of the 2D and G peak are plotted against each other, as illustrated in figure 6(b). Since the two peaks shift differently as function of doping and strain, the slopes of the distributions can be used to qualitatively evaluate the type of disorder in the system (strain and/or doping). A distribution parallel to the strain axis has a slope of 2.2 and is connected to biaxial strain whereas a distribution along the doping axis has a slope ranging between 0.3 and 0.7 depending on both their charge carrier type and the substrate [83, 112].

## 5.2. Results of spatially-resolved Raman spectroscopy

Raman measurements were performed with the same setup as for the characterization of the hBN crystals and films, using a grating of 1200 lines mm<sup>-1</sup>. Figures 7(f)–(j) show Raman maps of the graphene 2D linewidth for the regions highlighted with black dashed rectangles in the optical images in figures 7(a)–(e) for each BN source, respectively. The corresponding histograms are shown in figures 7(k)–(o) of a selected region of interest, highlighted with a dashed rectangle in the corresponding panel in figures 7(f)–(j). The color scale is the same for all maps. Regions of a higher 2D linewidth within a stack may either result from bubbles (hydrocarbons) that are trapped at the interface between hBN and graphene or may be related to regions with multilayers. Residual hydrocarbons most likely originate from tape residues during exfoliation or from the polymer used for stacking [113–115]. The latter is a commonly known challenge when using polymer-based dry-transfer techniques. We observe the formation of bubbles for all stacks produced in this study.

Comparison of the contamination-free regions of the 2D FWHM maps reveals the lowest  $\Gamma_{2D}$  values for graphene on APHT-hBN (figures 7(f)–(g)), followed by PCF-grown crystals (figure 7(h)) and then the BN films (figures 7(i)–(j)). The corresponding histograms in figures 7(k)–(o) enable the quantitative evaluation of the 2D FWHM maps. The maximum of the statistical distribution ranges from 16.5 cm<sup>-1</sup> for APHT-grown crystals, over 18 cm<sup>-1</sup> for PCF-grown crystals to values larger than 20 cm<sup>-1</sup> for BN films. We identify the peak position of the 2D linewidth distribution as a robust and sensitive quantity to evaluate the interface quality of the underlying BN, in line with previous works [80, 84]. We conclude that the degree of strain variations in graphene is lowest for the APHT hBN crystals, which shows that they have the highest interface quality (flatness) among the studied BN.

The respective  $\omega_{2D}$  vs  $\omega_G$  scatter plots are shown in figures 7(p)–(t), where the color code corresponds to the FWHM of the 2D peak. For the stack presented in the first row of figure 7 we chose a region with a spatially homogeneous and low 2D FWHM. The corresponding 2D vs G peak position distribution shows a strong clustering along the 2.2 strain axis indicating very small strain variations and negligible doping. For the sample in the second row, the distribution with the lowest 2D linewidth (blue data points) is again mainly distributed along the strain axis. However, areas with inclusion (bubbles) exhibit larger 2D linewidths (green, yellow and reddish color) with a distribution outside the strain axis, which is probably due to larger doping. The effect of doping on

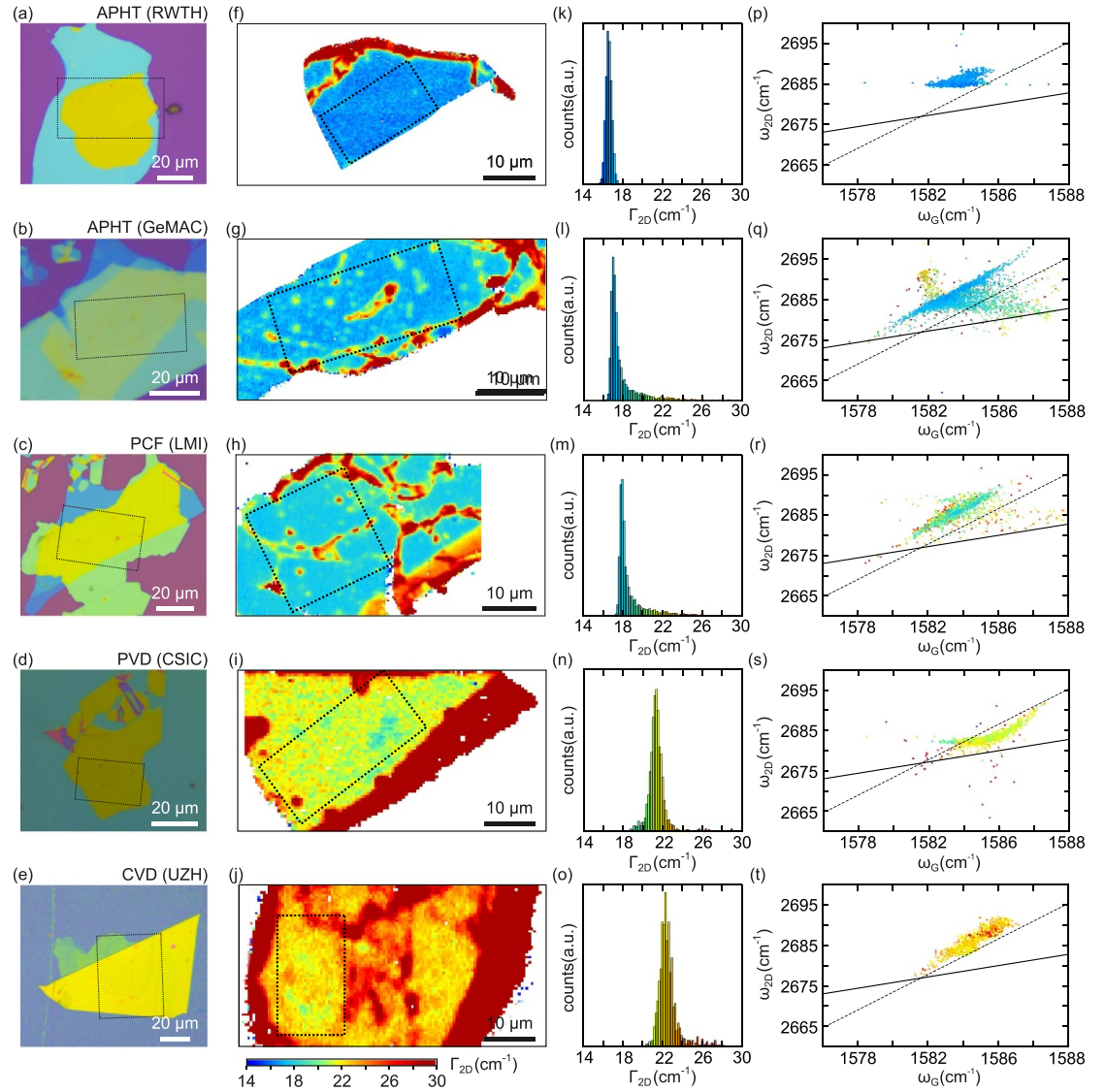


**Figure 7.** Optical microscopy images and Raman spectroscopy of dry-transferred hBN/graphene heterostructures. (a)–(e) Optical microscope images of one representative stack for each BN source, namely the APHT-hBN from RWTH and GeMaC, the PCF-hBN from LMI, the PVD grown BN film from CSIC and the transferred CVD hBN from UZH. (f)–(j) Spatially-resolved Raman map of the 2D FWHM of graphene of the region highlighted as a dashed black rectangle in the optical images in (a)–(e). (k)–(o) Statistical representation of the 2D FWHM extracted from the region highlighted as a dashed rectangle in the corresponding Raman maps shown in (f)–(j). (p)–(t) The 2D peak position vs G peak position. Each point is color coded with the FWHM of the 2D peak. The dashed line corresponds to the expected random strain distribution with a slope of 2.2 (see text), while the solid line corresponds to the expected doping distribution with a slope of 0.7.

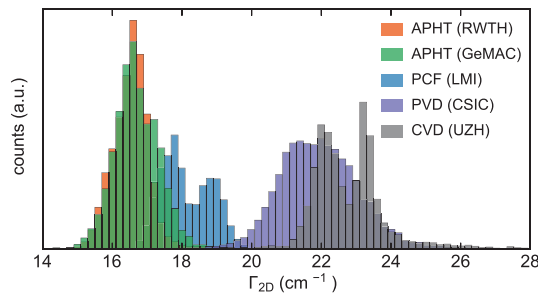


**Figure 8.** Distributions of the graphene 2D peak FWHM for all fabricated and evaluated heterostacks, combined in a single histogram for each BN source.

the peak positions is most clearly seen for the PVD-grown BN shown in the fourth row of figure 7. The peak positions show a curved distribution that results from both strain and doping.

To go beyond the evaluation of the comparison of representative examples, we plot the graphene 2D linewidth of high-quality regions of all evaluated samples in a combined histogram in figure 8. For the APHT-grown crystals we observe narrow distributions of the graphene 2D linewidth with the maximum at  $16.5 \text{ cm}^{-1}$ , demonstrating an excellent and reproducible interface quality between graphene and hBN over a number of 20 different heterostructures

with hBN crystals taken from different batches. The histogram distribution of the PCF-crystals shows a broader distribution ranging from  $17.5\text{ cm}^{-1}$  to  $19\text{ cm}^{-1}$  indicating a larger amount of strain variations, and when evaluating different stacks, we additionally observe a larger sample-to sample variation in the 2D linewidth distribution.

While the analysis of the free exciton lifetime  $\tau_{\text{CL}}$  in figure 2 shows slightly shorter lifetimes for RWTH-APHT crystals compared to the GEMaC-APHT crystals there are no differences in the amount of nm-strain variations of encapsulated graphene as inferred from Raman spectroscopy. In contrast, the broader and shifted graphene 2D linewidth distribution of heterostacks fabricated by the PCF crystals seems to be related to their shorter exciton lifetimes. As the graphene 2D linewidth is connected to nm-strain variations caused by the roughness of the substrate surface, we conclude that the defect concentration in the PCF-grown crystals is so high that it affects the electronic properties of graphene. Further, this quantity allows us to compare various substrates independent on their crystal nature to each other.

## 6. Processing into Hall bar structures

We next determine the key quantity of interest, the charge carrier mobility of graphene, and link it to the Raman 2D linewidths of graphene and the free exciton lifetimes of the BN substrate. For this purpose, the fabricated heterostructures are patterned into Hall bar devices and electrically contacted to perform gate-dependent charge transport measurements. For this study, we established a reproducible fabrication process yielding a high homogeneity of the electronic quality of graphene within a device as well as a high throughput of functioning contacts. For all devices we applied the same fabrication routine.

A simplified overview of the various processing steps is shown in figure 9(e). First, the Hall bar structure is defined by electron beam lithography (EBL) (step 1). Subsequently, 30 nm aluminum (Al) is deposited using electron beam evaporation with a rate of  $0.1\text{ nm s}^{-1}$  (step 2) and after lift-off we remain with the final Hall-bar structure protected by the Al hard mask (step 3). The structure is subsequently etched using atomic layer etching (Oxford Plasma Pro 100) using  $\text{Ar/SF}_6$  with a flow rate of 5/20 sccm and HF power of 50 W and a 5 s oxygen etch pulse. The Al is chemically removed using tetramethylammonium hydroxide (TMAH) (step 4). The contacts to the Hall bar are defined in a second EBL step (step 5) and 5 nm/70 nm of Cr/Au is evaporated, with a rate of  $0.2\text{ nm s}^{-1}$  and  $0.5\text{ nm s}^{-1}$  (step 6). An optical microscope image of a representative, structured and contacted device is shown in figure 9(b).

At this point, it is important to note that we have taken particular care to minimize the time between the individual processing steps. The etching, the subsequent second lithography step and the evaporation of Cr/Au was performed within the same day. By fabricating many devices, we have clear evidence that the time window between etching into the Hall bar structure where we expose the edges of graphene to air and the deposition of the side contacts to graphene should be minimized. For all devices, this time window was below 4 h.

### 6.1. Influence of processing on the electronic properties of graphene

In this section we discuss the impact of the Hall bar processing onto the mechanical and electronic quality of the devices by using spatially-resolved Raman spectroscopy. In figure 9 we show a representative device PCF (LMI), with an optical image of the stack in panel (a) and the final device in panel (b). Figures 9(c) and (d) depict spatially-resolved Raman maps of the graphene 2D linewidth of the heterostructure before and after processing, respectively. The black rectangle in figure 9(c) illustrates the region chosen for the Hall-bar patterning, and only the Raman data from this region are used for comparison with the final Hall bar. The respective histogram is shown in figure 9(f) (green data). A comparison of the two maps in figures 9(c) and (d) shows: (i) an overall increases in the Raman 2D FWHM in the center of the Hall bar, which leads to a shift of the respective histogram (red data in figure 9(f)) towards higher wavenumbers and (ii) a strong increase in linewidth towards the edges of the Hall bar (reddish color in figure 9(d) that is seen as a tail in the histogram extending to values above  $20\text{ cm}^{-1}$ ). This finding could be linked to mechanical stress that occurs during the fabrication steps. The different temperatures in the fabrication process, e.g. after baking the resist for lithography or during etching, can lead to stress due to the different thermal expansion coefficients of the materials within the stack and the substrate.

Considering the Raman 2D and G peak positions in figure 9(g), we clearly observe a red shift of the positions along the 2.2 strain line for the stack after fabrication. This cloud (red data points) has shifted towards phonon frequencies closer to the point related to that of ‘pristine’ graphene [83], suggesting that strain release may have occurred during the device fabrication. We only show one example here, but this finding is observed in many different samples, regardless of the type of BN used. A more detailed investigation is beyond the scope of this paper and future works focusing on the monitoring of different fabrication steps are necessary to draw clearer conclusions.

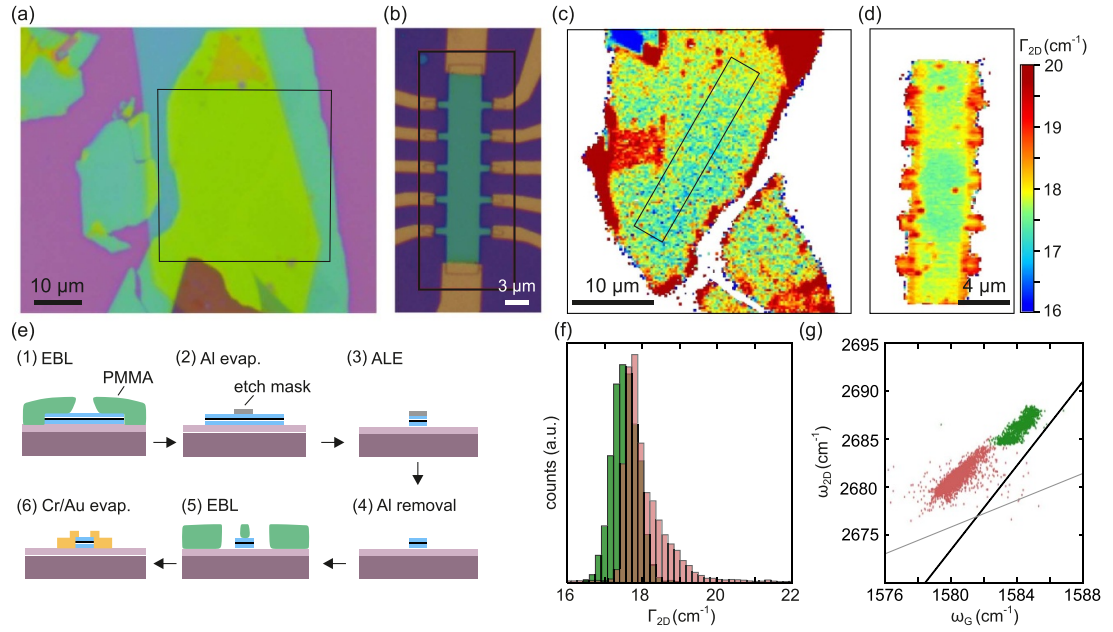


**Figure 9.** Fabrication of Hall-bar structures from van der Waals (vdW) heterostructures. (a) Optical microscope image of hBN/graphene/hBN vdW heterostructure. The black rectangle denotes the area mapped by Raman spectroscopy shown in panel (c). (b) Optical microscope image of the patterned and contacted Hall bar. (c) Spatially-resolved Raman map of the graphene 2D FWHM. The black rectangle corresponds to the position where the Hall bar is placed. (d) Spatially-resolved Raman map of the 2D FWHM of the finished Hall bar. (e) Schematic of the process overview for Hall bar structures. (1) Electron beam lithography to define the Hall bar structure, followed by (2) electron beam evaporation of aluminum and (3) subsequent atomic layer etching. After chemical etching of the aluminum in TMAH (4) the contacts are defined in a second EBL step (5) and the Hall bar is finally contacted by Cr/Au evaporation (6). (f) Histogram of the Raman 2D peak FWHM before (green) and after (red) Hall bar fabrication. (g) Scatter plot of the graphene 2D vs G peak position before and after Hall bar fabrication. The black line shows the expected distribution for biaxial strain (slope = 2.2) and the grey line for doping (slope = 0.7).

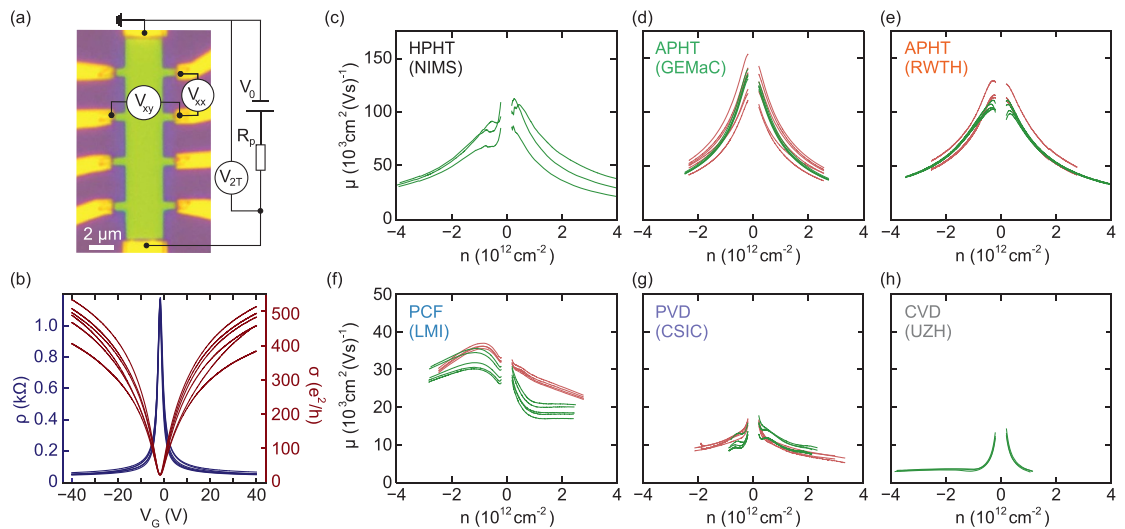


**Figure 10.** Charge transport measurements on graphene/BN Hall bars. (a) Optical image of a representative Hall bar structure with a schematic representation of the electrical wiring. (b) Four-terminal resistivity (conductivity) as function of the silicon back gate voltage. (c)–(g) Extracted Drude mobilities as function of charge carrier density for HPHT-NIMS, APHT-RWTH, RWTH-GEMaC, PCF-LMI, PVD-CSIC and CVD-UZH (wet-transferred), respectively. Traces of the same color correspond to multiple regions measured within the same device. Different colors correspond to different devices.



## 6.2. Room temperature charge carrier mobilities

The individual Hall bars with the different BN substrates were fabricated in heterostack regions of the lowest possible and homogeneous graphene Raman 2D FWHM (as an example, see black rectangle in figure 9(c)). All charge transport measurements were taken at room temperature under vacuum. An example of a Hall bar with the measurement scheme is depicted in figure 10(a). We use an AC voltage  $V_0 = 1$  V at a frequency of 77 Hz and a series resistance of  $R_p = 1$  M $\Omega$  to pass a constant current of  $I = 1$   $\mu$ A between the source and drain contact. The four-terminal voltage drop is measured for different regions along the graphene transport channel, labelled as  $V_{xx}$  in figure 10(a) for the upper region as an example. This voltage drop converts to the resistivity (1/conductivity) following  $\rho = 1/\sigma = W/L \cdot V_{xx}/I$ , where  $L$  is the distance between the contacts and  $W$  the width of the transport channel.

Figure 10(b) shows the gate dependent resistivity and conductivity for an APHT device (red traces in panel (d)). For all measured regions, the conductivity  $\sigma$  reaches at least  $400e^2/h$  at large gate voltages, i.e. large charge carrier densities, which is mainly limited by electron–phonon scattering [20]. Importantly, and in contrast to previous studies, we observe homogeneous transport properties along the graphene channel and a high yield of functioning contacts (larger than 90 %). While the electronic homogeneity is likely due to the pre-selection of the regions via Raman mapping, we link the high throughput of functioning contacts to the decreased time between the etching (i.e. exposing of graphene contact areas) and evaporation of the Cr/Au.

The charge carrier density  $n$  is extracted from Hall effect measurements. It is connected to the gate voltage by  $n = \alpha(V_G - V_G^0)$ , where  $V_G^0$  is the position of the charge neutrality point, i.e. the voltage of the Dirac peak, and  $\alpha$  is the gate lever arm. The carrier mobilities  $\mu = \sigma/(ne)$  of graphene with the different BN substrates are shown in figures 10(c)–(h) for each BN source individually. As a reference, we show transport data for a Hall bar device where we used HPHT hBN (NIMS) (see figure 10(c)). For each device, multiple regions were measured. Traces of the same color are from different regions of the same device. There are only small variations in transport characteristics within a single device but also between different devices fabricated from the same BN source. This finding further confirms a robust and reliable processing routine, which was developed as part of the benchmarking study. For devices built by APHT hBN we measure the highest charge carrier mobilities exceeding  $80\,000\text{ cm}^2(\text{Vs})^{-1}$  at a charge carrier density of  $|n| = 1 \times 10^{12}\text{ cm}^{-2}$  (see figures 10(c) and (d)). These values are fully in line with state of the art

high-mobility graphene devices using HPHT hBN [20] (see also figure 10(c)) or APHT hBN from other sources [22–24]. We therefore highlight the viability of APHT hBN crystals as a true alternative to HPHT hBN crystals, for high-performance graphene devices. For the PCF-grown crystals in figure 10(f), we observe a carrier mobility of up to  $30\,000\text{ cm}^2(\text{Vs})^{-1}$  at  $|n| = 1 \times 10^{12}\text{ cm}^{-2}$ . The lower charge carrier mobility of graphene encapsulated in PCF-grown hBN, when compared to APHT hBN, is fully consistent with our two previous observations, a shorter free exciton lifetime and a higher 2D linewidth of graphene encapsulated in PCF-grown hBN crystals. The relation between an increase in graphene 2D linewidth and a decrease in charge carrier mobility is understood in terms of increased electron backscattering due to the stronger nm-strain variations [82]. For the PVD grown BN film (figure 10(g)) we extract charge carrier mobilities over  $10\,000\text{ cm}^2(\text{Vs})^{-1}$  at  $n = 1 \times 10^{12}\text{ cm}^{-2}$ , while we achieve mobilities around  $4000\text{ cm}^2(\text{Vs})^{-1}$  at  $n = 1 \times 10^{12}\text{ cm}^{-2}$  for the CVD-grown and wet-transferred films (figure 10(h)).

## 7. Discussion

In figure 11, we summarize the main results of the BN benchmarking study: (a) room temperature charge carrier mobility vs carrier density and carrier mobilities at  $n = 1 \times 10^{12}\text{ cm}^{-2}$  vs (b) free exciton lifetime of hBN, (c)  $\Gamma_{E_{2g}}$  of hBN and (d) graphene 2D linewidth of all BN substrates. In figure 11(a) we show the transport traces for the region of highest mobility for each device shown in figures 10(c)–(h). As mentioned above, APHT grown hBN allows for equally high graphene mobilities as achieved for HPHT-grown hBN crystals. These hBN sources are of high relevance for many research groups, who are interested in high quality hBN crystals for fundamental research. The PCF-grown crystals, following another route of hBN crystal growth, allow for mobilities up to  $30\,000\text{ cm}^2(\text{Vs})^{-1}$  at  $n = 1 \times 10^{12}\text{ cm}^{-2}$ , demonstrating the great potential of new synthesis routes for the production of high quality hBN crystals. One aim of this synthesis route is to satisfy the increasing demand of hBN crystals from many research groups. However, these approaches to grow high quality hBN crystals are not scalable, because they cannot be easily combined with technologically relevant substrates and the desired thicknesses can only be achieved via mechanical exfoliation. Scalable methods for growing BN are therefore needed to unlock the full potential of graphene-based electronics in future nanoelectronic devices.

In this respect, the PVD growth method is most promising because (i) it allows the growth of

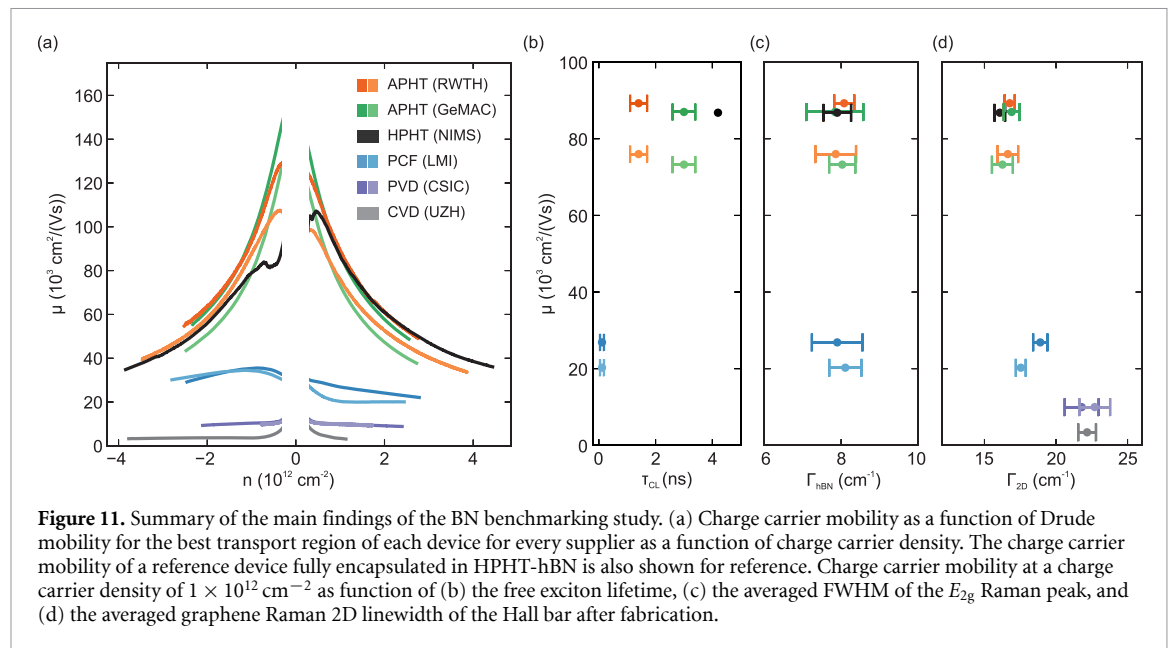


**Figure 11.** Summary of the main findings of the BN benchmarking study. (a) Charge carrier mobility as a function of Drude mobility for the best transport region of each device for every supplier as a function of charge carrier density. The charge carrier mobility of a reference device fully encapsulated in HPHT-hBN is also shown for reference. Charge carrier mobility at a charge carrier density of  $1 \times 10^{12} \text{ cm}^{-2}$  as function of (b) the free exciton lifetime, (c) the averaged FWHM of the  $E_{2g}$  Raman peak, and (d) the averaged graphene Raman 2D linewidth of the Hall bar after fabrication.

tens of nanometer thick films with very low surface roughness and (ii) it can be deposited directly onto Si/SiO<sub>2</sub> substrates. The large BN thickness screens disorder from the silicon substrates, while the deposition on the target substrates prevents the need for large scale layer transfer. Most importantly, the PVD-grown BN allows for room temperature carrier mobilities of graphene exceeding  $10000 \text{ cm}^2/(\text{Vs})^{-1}$  at  $n = 1 \times 10^{12} \text{ cm}^{-2}$ . We conclude that the low temperature PVD growth process of BN on SiO<sub>2</sub> is a promising platform for achieving scalable BN substrates not only for graphene, but also for other 2D materials.

If we compare the charge carrier mobility with the Raman 2D FWHM we see a clear trend of decreasing mobility with increasing 2D FWHM. This is in good agreement with the finding that nm-scale strain variations are the limitation for high charge carrier mobilities [82] and shows that the graphene Raman 2D FWHM is a good measure for benchmarking as used in the ICE TS 62 607-6-6 key control characteristics [116]. Whereas we do not find a correlation between the FWHM of the hBN Raman peak and the charge carrier mobility we observe a clear correlation between the CL lifetime and the mobility, as shown in figure 11(b). We observe that we need CL lifetimes of over 1 ns to achieve charge carrier mobilities in the range of  $80000 \text{ cm}^2/(\text{Vs})^{-1}$  at  $n = 1 \times 10^{12} \text{ cm}^{-2}$ . For CL lifetimes of 100 ps we achieve charge carrier mobilities up to  $30000 \text{ cm}^2/(\text{Vs})^{-1}$ . The interface quality is therefore connected to the hBN crystal quality, i.e. the number of defects, in a sensitive way.

In conclusion, we have presented a comprehensive study of the electronic properties of graphene on different boron nitride substrates using a newly developed reproducible processing routine. We have

shown the complete process from boron nitride synthesis, over its optical characterization, to the optical and electronic characterization of graphene after encapsulation and Hall bar fabrication. We identify the Raman spectrum of BN as a valuable measure for distinguishing hBN in the high crystallinity limit from BN films, but we also point out the limitations of the Raman analysis when comparing high-quality hBN crystals. In this respect, time-resolved cathodoluminescence has a clear advantage over Raman spectroscopy when evaluating the as-grown quality of hBN, as the probing of the free exciton lifetime is very sensitive to the defects in hBN. The fabrication of graphene-based heterostructures on BN substrates demonstrates the high sensitivity of graphene to the environment, allowing graphene to be used as a sensitive detector of the substrate and interface quality. Variations in the quality of the graphene-BN interface are directly reflected in a broadening of the graphene Raman 2D peak. This broadening has a direct effect on the carrier mobility, i.e. the mobility is inversely proportional to the peak of the 2D linewidth distribution of graphene. It is therefore advisable to characterize the Raman 2D linewidth distribution of the finished heterostructure prior to any processing. In terms of benchmarking we find that a CL lifetime larger than 1 ns is sufficient for high hBN crystal quality and high graphene-hBN interface qualities with low nm strain variations in graphene, which is essential for fundamental studies on highest mobility graphene-based devices. For scalable approaches we see that a graphene Raman 2D linewidth below  $22 \text{ cm}^{-1}$  is necessary to achieve charge carrier mobilities over  $10000 \text{ cm}^2/(\text{Vs})^{-1}$ . PVD-grown BN films, therefore, offer a promising platform for scalable high mobility graphene devices.

## Data availability statement

The data supporting the findings of this study are available in a Zenodo repository under, <https://doi.org/10.5281/zenodo.13684712> [117].

## Acknowledgments


This project has received funding from the European Union's Horizon 2020 research and innovation programme under Grant Agreement No. 881603 (Graphene Flagship), T O, S B, P S, C S, and B B acknowledge support from the European Research Council (ERC) under Grant Agreement No. 820254, and the Deutsche Forschungsgemeinschaft (DFG, German Research Foundation) under Germany's Excellence Strategy—Cluster of Excellence Matter and Light for Quantum Computing (ML4Q) EXC 2004/1—390534769. H Y C was supported by a SPARK grant of the Swiss National Science Foundation (Grant No. CRSK-2\_220582). A H acknowledges a Forschungskredit of the University of Zürich (Grant No. FK-20-206 114). K W and T T acknowledge support from the JSPS KAKENHI (Grant Numbers 21H05233 and 23H02052) and World Premier International Research Center Initiative (WPI), MEXT, Japan.

## ORCID iDs

Taoufiq Ouaj  <https://orcid.org/0009-0003-8316-523X>

Christophe Arnold  <https://orcid.org/0000-0001-5540-8589>

Jon Azpeitia  <https://orcid.org/0000-0003-4542-9735>

Julien Barjon  <https://orcid.org/0000-0003-1749-2980>

José Cascales  <https://orcid.org/0009-0005-3433-8063>

Huanyao Cun  <https://orcid.org/0000-0002-5225-9861>

David Esteban  <https://orcid.org/0009-0006-0167-1545>

Mar Garcia-Hernandez  <https://orcid.org/0000-0002-5987-0647>

Thomas Greber  <https://orcid.org/0000-0002-5234-1937>

Ignacio Jiménez  <https://orcid.org/0000-0001-5605-3185>

Catherine Journet  <https://orcid.org/0000-0002-3328-317X>

Paul Kögerler  <https://orcid.org/0000-0001-7831-3953>

Annick Loiseau  <https://orcid.org/0000-0002-1042-5876>

Camille Maestre  <https://orcid.org/0000-0002-7911-3758>

Marvin Metzelaars  <https://orcid.org/0000-0002-3529-557X>

Philipp Schmidt  <https://orcid.org/0000-0002-1278-1727>

Christoph Stampfer  <https://orcid.org/0000-0002-4958-7362>

Ingrid Stenger  <https://orcid.org/0000-0002-8917-5776>

Takashi Taniguchi  <https://orcid.org/0000-0002-1467-3105>

Bérangère Toury  <https://orcid.org/0000-0001-5889-0796>

Kenji Watanabe  <https://orcid.org/0000-0003-3701-8119>

Bernd Beschoten  <https://orcid.org/0000-0003-2359-2718>

## References

- [1] Meng J, Wang D, Cheng L, Gao M and Zhang X 2019 Recent progress in synthesis, properties and applications of hexagonal boron nitride-based heterostructures *Nanotechnology* **30** 074003
- [2] Schué L, Stenger I, Fossard F, Loiseau A and Barjon J 2016 Characterization methods dedicated to nanometer-thick hBN layers *2D Mater.* **4** 1–11
- [3] Backes C *et al* 2020 Production and processing of graphene and related materials *2D Mater.* **7** 022001
- [4] Naclerio A E and Kidambi P R 2023 A review of scalable hexagonal boron Nitride (h-BN) synthesis for present and future applications *Adv. Mater.* **35** 2207374
- [5] Watanabe K, Taniguchi T and Kanda H 2004 Direct-bandgap properties and evidence for ultraviolet lasing of hexagonal boron nitride single crystal *Nat. Mater.* **3** 404–9
- [6] Kubota Y, Watanabe K, Tsuda O and Taniguchi T 2007 Deep ultraviolet light-emitting hexagonal boron nitride synthesized at atmospheric pressure *Science* **317** 932–4
- [7] Bourrellier R, Meuret S, Tararan A, Stéphan O, Kociak M, Tizei L H G and Zobelli A 2016 Bright UV single photon emission at point defects in h-BN *Nano Lett.* **16** 4317–21
- [8] Grosso G, Moon H, Lienhard B, Ali S, Efetov D K, Furchi M M, Jarillo-Herrero P, Ford M J, Aharonovich I and Englund D 2017 Tunable and high-purity room temperature single-photon emission from atomic defects in hexagonal boron nitride *Nat. Commun.* **8** 705
- [9] Martínez L J, Pelini T, Waselowski V, Maze J R, Gil B, Cassaboies G and Jacques V 2016 Efficient single photon emission from a high-purity hexagonal boron nitride crystal *Phys. Rev. B* **94** 121405(R)
- [10] Fournier C *et al* 2021 Position-controlled quantum emitters with reproducible emission wavelength in hexagonal boron nitride *Nat. Commun.* **12** 3779
- [11] Lindsay L and Broido D A 2011 Enhanced thermal conductivity and isotope effect in single-layer hexagonal boron nitride *Phys. Rev. B* **84** 155421
- [12] Yuan C, Li J, Lindsay L, Cherns D, Pomeroy J W, Liu S, Edgar J H and Kuball M 2019 Modulating the thermal conductivity in hexagonal boron nitride via controlled boron isotope concentration *Commun. Phys.* **2** 43
- [13] Xue J, Sanchez-Yamagishi J, Bulmash D, Jacquod P, Deshpande A, Watanabe K, Taniguchi T, Jarillo-Herrero P and LeRoy B J 2011 Scanning tunnelling microscopy and spectroscopy of ultra-flat graphene on hexagonal boron nitride *Nat. Mater.* **10** 282–5

- [14] Woods C R *et al* 2014 Commensurate–incommensurate transition in graphene on hexagonal boron nitride *Nat. Phys.* **10** 451–6
- [15] Britnell L *et al* 2012 Electron tunneling through ultrathin boron nitride crystalline barriers *Nano Lett.* **12** 1707–10
- [16] Sharpe A L, Fox E J, Barnard A W, Finney J, Watanabe K, Taniguchi T, Kastner M A and Goldhaber-Gordon D 2019 Emergent ferromagnetism near three-quarters filling in twisted bilayer graphene *Science* **365** 605–8
- [17] Tebbe D, Schütte M, Watanabe K, Taniguchi T, Stampfer C, Beschoten B and Waldecker L 2023 Tailoring the dielectric screening in WS<sub>2</sub> graphene heterostructures *npj 2D Mater. Appl.* **7** 29
- [18] Tebbe D, Schütte M, Watanabe K, Taniguchi T, Stampfer C, Beschoten B and Waldecker L 2024 Distance dependence of the energy transfer mechanism in WS<sub>2</sub>-graphene heterostructures *Phys. Rev. Lett.* **132** 196902
- [19] Dean C R *et al* 2010 Boron nitride substrates for high-quality graphene electronics *Nat. Nanotechnol.* **5** 722–6
- [20] Wang L *et al* 2013 One-dimensional electrical contact to a two-dimensional material *Science* **342** 614–7
- [21] Banszerus L, Schmitz M, Engels S, Dauber J, Oellers M, Haupt F, Watanabe K, Taniguchi T, Beschoten B and Stampfer C 2015 Ultrahigh-mobility graphene devices from chemical vapor deposition on reusable copper *Sci. Adv.* **1** e1500222
- [22] Onodera M, Taniguchi T, Watanabe K, Isayama M, Masubuchi S, Moriya R and Machida T 2020 hexagonal boron nitride synthesized at atmospheric pressure using metal alloy solvents: evaluation as a substrate for 2D materials *Nano Lett.* **20** 735–40
- [23] Sonntag J Li J, Plaud A, Loiseau A, Barjon J, Edgar J H and Stampfer C 2020 Excellent electronic transport in heterostructures of graphene and monoisotopic boron-nitride grown at atmospheric pressure *2D Mater.* **7** 031009
- [24] Ouaj T, Kramme L, Metzelaars M, Li J, Watanabe K, Taniguchi T, Edgar J H, Beschoten B, Kögerler P and Stampfer C 2023 Chemically detaching hBN crystals grown at atmospheric pressure and high temperature for high-performance graphene devices *Nanotechnology* **34** 475703
- [25] Ajayi O A *et al* 2017 Approaching the intrinsic photoluminescence linewidth in transition metal dichalcogenide monolayers *2D Mater.* **4** 031011
- [26] Ye Z *et al* 2018 Efficient generation of neutral and charged biexcitons in encapsulated WSe<sub>2</sub> monolayers *Nat. Commun.* **9** 3718
- [27] Raja A *et al* 2019 Dielectric disorder in two-dimensional materials *Nat. Nanotechnol.* **14** 832–7
- [28] Cadiz F *et al* 2017 Excitonic Linewidth Approaching the Homogeneous Limit in MoS<sub>2</sub>-Based van der Waals Heterostructures *Phys. Rev. X* **7** 021026
- [29] Ersfeld M *et al* 2020 Unveiling Valley Lifetimes of Free Charge Carriers in Monolayer WSe<sub>2</sub> *Nano Lett.* **20** 3147–54
- [30] Shi Q, Shih E-M, Gustafsson M V, Rhodes D A, Kim B, Watanabe K, Taniguchi T, Papić Z, Hone J and Dean C R 2020 Odd- and even-denominator fractional quantum Hall states in monolayer WSe<sub>2</sub> *Nat. Nanotechnol.* **15** 569–73
- [31] Volmer F *et al* 2023 Twist angle dependent interlayer transfer of valley polarization from excitons to free charge carriers in WSe<sub>2</sub>/MoSe<sub>2</sub> heterobilayers *npj 2D Mater. Appl.* **7** 58
- [32] Kundu B *et al* 2024 Electrically controlled excitons, charge transfer induced trions and narrowband emitters in MoSe<sub>2</sub>-WSe<sub>2</sub> lateral heterostructure *Nano Lett.* **2024** 14615–24
- [33] Eich M *et al* 2018 Coupled quantum dots in bilayer graphene *Nano Lett.* **18** 5042–8
- [34] Banszerus L, Frohn B, Epping A, Neumaier D, Watanabe K, Taniguchi T and Stampfer C 2018 Gate-defined electron–hole double dots in bilayer graphene *Nano Lett.* **18** 4785–90
- [35] Icking E *et al* 2022 Transport spectroscopy of ultraclean tunable band gaps in bilayer graphene *Adv. Electron. Mater.* **8** 2200510
- [36] Icking E, Emmerich D, Watanabe K, Taniguchi T, Beschoten B, Lemme M C, Knoch J and Stampfer C 2024 Ultrasteep slope cryogenic FETs based on bilayer graphene *Nano Lett.* **24** 11454–61
- [37] Taniguchi T and Watanabe K 2007 Synthesis of high-purity boron nitride single crystals under high pressure by using Ba–BN solvent *J. Cryst. Growth* **303** 525–9
- [38] Zhigadlo N D 2014 Crystal growth of hexagonal boron nitride (hBN) from Mg–B–N solvent system under high pressure *J. Cryst. Growth* **402** 308–11
- [39] Fukunaga O, Nakano S and Taniguchi T 2022 Experimental results on the high-pressure phase diagram of boron nitride *Jpn. J. Appl. Phys.* **61** 125502
- [40] Kubota Y, Watanabe K, Tsuda O and Taniguchi T 2008 Hexagonal boron nitride single crystal growth at atmospheric pressure using Ni–Cr solvent *Chem. Mater.* **20** 1661–3
- [41] Hoffman T B, Clubine B, Zhang Y, Snow K and Edgar J H 2014 Optimization of Ni–Cr flux growth for hexagonal boron nitride single crystals *J. Cryst. Growth* **393** 114–8
- [42] Edgar J H, Hoffman T B, Clubine B, Currie M and Jiang H X 2014 Characterization of bulk hexagonal boron nitride single crystals grown by the metal flux technique *J. Cryst. Growth* **403** 110–3
- [43] Liu S, He R, Ye Z, Du X, Lin J, Jiang H, Liu B and Edgar J H 2017 Large-scale growth of high-quality hexagonal boron nitride crystals at atmospheric pressure from an Fe–Cr flux *Cryst. Growth Des.* **17** 4932–5
- [44] Liu S, He R, Xue L, Li J, Liu B and Edgar J H 2018 Single crystal growth of millimeter-sized monoisotopic hexagonal boron nitride *Chem. Mater.* **30** 6222–5
- [45] Zhang S-Y, Xu K, Zhao X-K, Shao Z-Y and Wan N 2019 Improved hBN single-crystal growth by adding carbon in the metal flux *Cryst. Growth Des.* **19** 6252–7
- [46] Li J *et al* 2020 Hexagonal boron nitride single crystal growth from solution with a temperature gradient *Chem. Mater.* **32** 5066–72
- [47] Li J *et al* 2021 Hexagonal boron nitride crystal growth from iron, a single component flux *ACS Nano* **15** 7032–9
- [48] Li J *et al* 2020 Single crystal growth of monoisotopic hexagonal boron nitride from a Fe–Cr flux *J. Mater. Chem. C* **8** 9931–5
- [49] Li Y *et al* 2021 Synthesis of centimeter-scale high-quality polycrystalline hexagonal boron nitride films from Fe fluxes *Nanoscale* **13** 11223–31
- [50] Zhang N, Yang N, Wang W, Zhong X and Chen X 2021 Growth of hexagonal boron nitride crystals at atmospheric pressure from CuCr flux *J. Cryst. Growth* **562** 126074
- [51] Li Y, Garnier V, Steyer P, Journet C and Toury B 2020 Millimeter-scale hexagonal boron nitride single crystals for nanosheet generation *ACS Appl. Nano Mater.* **3** 1508–15
- [52] Maestre C *et al* 2022 From the synthesis of hBN crystals to their use as nanosheets in van der Waals heterostructures *2D Mater.* **9** 035008
- [53] Chubarov M, Pedersen H, Höglberg H, Filippov S, Engelbrecht J, O’Connell J and Henry A 2013 Characterization of boron nitride thin films *2013 Conf. on Lasers and Electro-Optics Pacific Rim (CLEOPR)* (IEEE) pp 2013–04
- [54] Jang A-R *et al* 2016 Wafer-scale and Wrinkle-Free epitaxial growth of single-orientated multilayer hexagonal boron nitride on sapphire *Nano Lett.* **16** 3360–6
- [55] Lee J S *et al* 2018 Wafer-scale single-crystal hexagonal boron nitride film via self-collimated grain formation *Science* **362** 817–21



- [56] Asgari M *et al* 2022 Terahertz photodetection in scalable single-layer-graphene and hexagonal boron nitride heterostructures *Appl. Phys. Lett.* **121** 031103
- [57] Calandrini E *et al* 2023 Near- and far-field observation of phonon polaritons in wafer-scale multilayer hexagonal boron nitride prepared by chemical vapor deposition *Adv. Mater.* **35** 2302045
- [58] Tailpied L, Andrieux-Ledier A, Fossard F, Mérot J-S, Decams J-M and Loiseau A 2024 Ni(111) Substrate engineering for the epitaxial chemical vapor deposition growth of wrinkle-free multilayer rhombohedral boron nitride films *Cryst. Growth Des.* **24** 7432–44
- [59] Kobayashi Y and Akasaka T 2008 Hexagonal BN epitaxial growth on (0001) sapphire substrate by MOVPE *J. Cryst. Growth* **310** 5044–7
- [60] Kobayashi Y, Kumakura K, Akasaka T and Makimoto T 2012 Layered boron nitride as a release layer for mechanical transfer of GaN-based devices *Nature* **484** 223–7
- [61] Li X, Sundaram S, El Gmili Y, Ayari T, Puybaret R, Patriarche G, Voss P L, Salvestrini J P and Ougazzaden A 2016 Large-area two-dimensional layered hexagonal boron nitride grown on sapphire by metalorganic vapor phase epitaxy *Cryst. Growth Des.* **16** 3409–15
- [62] Jeong H *et al* 2019 Wafer-scale and selective-area growth of high-quality hexagonal boron nitride on Ni(111) by metal-organic chemical vapor deposition *Sci. Rep.* **9** 5736
- [63] Cho Y-J *et al* 2016 Hexagonal boron nitride tunnel barriers grown on graphite by high temperature molecular beam epitaxy *Sci. Rep.* **6** 34474
- [64] Elias C *et al* 2019 Direct band-gap crossover in epitaxial monolayer boron nitride *Nat. Commun.* **10** 2639
- [65] Heilmann M, Prikhodko A S, Hanke M, Sabelfeld A, Borgardt N I and Lopes J M J 2020 Influence of proximity to supporting substrate on van der Waals epitaxy of atomically thin graphene/hexagonal boron nitride heterostructures *ACS Appl. Mater. Interfaces* **12** 8897–907
- [66] Rousseau A *et al* 2024 Spatially-resolved UV-C emission in epitaxial monolayer boron nitride *2D Mater.* **11** 025026
- [67] Caretti I and Jiménez I 2011 Composition and bonding structure of boron nitride  $B_{1-x}N_x$  thin films grown by ion-beam assisted evaporation *Chem. Phys. Lett.* **511** 235–40
- [68] Jiménez I, Torres R, Caretti I, Gago R and Albella J M 2012 A review of monolithic and multilayer coatings within the boron–carbon–nitrogen system by ion-beam-assisted deposition *J. Mater. Res.* **27** 743–64
- [69] Torres R, Caretti I, Serin V, Brun N, Radnócz G and Jiménez I 2014 Reversed texture in nanometric carbon/boron nitride multilayers *Carbon* **74** 374–8
- [70] Hong S *et al* 2020 Ultralow-dielectric-constant amorphous boron nitride *Nature* **582** 511–4
- [71] Sattari-Esfahlan S M *et al* 2023 Low-temperature direct growth of amorphous boron nitride films for high-performance nanoelectronic device applications *ACS Appl. Mater. Interfaces* **15** 7274–81
- [72] Martini L *et al* 2023 Scalable high-mobility Graphene/hBN heterostructures *ACS Appl. Mater. Interfaces* **15** 37794–801
- [73] Schué L, Berini B, Betz A C, Plaçais B, Ducastelle F, Barjon J and Loiseau A 2016 Dimensionality effects on the luminescence properties of hBN *Nanoscale* **8** 6986–93
- [74] Schué L, Sponza L, Plaud A, Bensalah H, Watanabe K, Taniguchi T, Ducastelle F, Loiseau A and Barjon J 2019 Bright luminescence from indirect and strongly bound excitons in h-BN *Phys. Rev. Lett.* **122** 067401
- [75] Roux S *et al* 2021 Radiative lifetime of free excitons in hexagonal boron nitride *Phys. Rev. B* **104** L161203
- [76] Cassaboïs G, Valvin P and Gil B 2016 Hexagonal boron nitride is an indirect bandgap semiconductor *Nat. Photon.* **10** 262–6
- [77] Rousseau A *et al* 2021 Monolayer boron nitride: hyperspectral imaging in the deep ultraviolet *Nano Lett.* **21** 10133–8
- [78] Reich S, Ferrari A C, Arenal R, Loiseau A, Bello I and Robertson J 2005 Resonant Raman scattering in cubic and hexagonal boron nitride *Phys. Rev. B* **71** 205201
- [79] Stenger I, Schué L, Boukhicha M, Berini B, Plaçais B, Loiseau A and Barjon J 2017 Low frequency Raman spectroscopy of few-atomic-layer thick hBN crystals *2D Mater.* **4** 031003
- [80] Banszerus L, Janssen H, Otto M, Epping A, Taniguchi T, Watanabe K, Beschoten B, Neumaier D and Stampfer C 2017 Identifying suitable substrates for high-quality graphene-based heterostructures *2D Mater.* **4** 025030
- [81] Caretti I and Jiménez I 2012 Influence of carbon content and nitrogen vacancies on the bonding structure and mechanical performance of graphite-like  $BC_xN$  thin films *J. Appl. Phys.* **112** 063525
- [82] Couto N J G, Costanzo D, Engels S, Ki D-K, Watanabe K, Taniguchi T, Stampfer C, Guinea F and Morpurgo A F 2014 Random strain fluctuations as dominant disorder source for high-quality on-substrate graphene devices *Phys. Rev. X* **4** 041019
- [83] Lee J E, Ahn G, Shim J, Lee Y S and Ryu S 2012 Optical separation of mechanical strain from charge doping in graphene *Nat. Commun.* **3** 1024
- [84] Neumann C *et al* 2015 Raman spectroscopy as probe of nanometre-scale strain variations in graphene *Nat. Commun.* **6** 8429
- [85] Vincent T, Panchal V, Booth T, Power S R, Jauho A-P, Antonov V and Kazakova O 2018 Probing the nanoscale origin of strain and doping in graphene-hBN heterostructures *2D Mater.* **6** 015022
- [86] Solozhenko V L and Turkevich V Z 1997 High pressure phase equilibria in the  $Li_3N$ -BN system: in situ studies *Mater. Lett.* **32** 179–84
- [87] Maestre C, Toury B, Steyer P, Garnier V and Journet C 2021 Hexagonal boron nitride: a review on selfstanding crystals synthesis towards 2D nanosheets *J. Phys. Mater.* **4** 044018
- [88] Sahni K, Ashuri M, Emami S, Kaduk J A, Németh K and Shaw L L 2018 On the synthesis of lithium boron nitride ( $Li_3BN_2$ ) *Ceram. Int.* **44** 7734–40
- [89] Schmitt A *et al* 2023 High-field  $1/f$  noise in hBN-encapsulated graphene transistors *Phys. Rev. B* **107** L161104
- [90] Verguts K *et al* 2017 Controlling water intercalation is key to a direct graphene transfer *ACS Appl. Mater. Interfaces* **9** 37484–92
- [91] Hemmi A *et al* 2014 High quality single atomic layer deposition of hexagonal boron nitride on single crystalline Rh(111) four-inch wafers *Rev. Sci. Instrum.* **85** 035101
- [92] Hemmi A, Cun H, Brems S, Huyghebaert C and Greber T 2021 Wafer-scale, epitaxial growth of single layer hexagonal boron nitride on Pt(111) *J. Phys. Mater.* **4** 044012
- [93] Cun H *et al* 2018 Centimeter-sized single-orientation monolayer hexagonal boron nitride with or without nanovoids *Nano Lett.* **18** 1205–12
- [94] Jiménez I, Jankowski A F, Terminello L J, Sutherland D G J, Carlisle J A, Doll G L, Tong W M, Shuh D K and Himpsel F J 1997 Core-level photoabsorption study of defects and metastable bonding configurations in boron nitride *Phys. Rev. B* **55** 12025–37
- [95] Caretti I and Jiménez I 2011 Point defects in hexagonal BN,  $BC_3$  and  $BC_xN$  compounds studied by x-ray absorption near-edge structure *J. Appl. Phys.* **110** 023511
- [96] Roux S *et al* 2024 Surface recombination and out-of-plane diffusivity of free excitons in hexagonal boron nitride *Phys. Rev. B* **109** 155305
- [97] Plaud A, Schué L, Watanabe K, Taniguchi T, Fossard F, Ducastelle F, Loiseau A and Barjon J 2019 Exciton-exciton annihilation in hBN *Appl. Phys. Lett.* **114** 232103
- [98] Geick R, Perry C H and Rupprecht G 1966 Normal modes in hexagonal boron nitride *Phys. Rev.* **146** 543–7
- [99] Cuscó R, Edgar J H, Liu S, Li J and Artús L 2020 Isotopic disorder: the prevailing mechanism in limiting the

- phonon lifetime in hexagonal BN *Phys. Rev. Lett.* **124** 167402
- [100] Gorbachev R V *et al* 2011 Hunting for monolayer boron nitride: optical and Raman signatures *Small* **7** 465–8
- [101] Uslu J-L *et al* 2024 An open-source robust machine learning platform for real-time detection and classification of 2D material flakes *Mach. Learn.: Sci. Technol.* **5** 015027
- [102] Nemanich R J, Solin S A and Martin R M 1981 Light scattering study of boron nitride microcrystals *Phys. Rev. B* **23** 6348–56
- [103] Song L *et al* 2010 Large scale growth and characterization of atomic hexagonal boron nitride layers *Nano Lett.* **10** 3209–15
- [104] Shi Y *et al* 2010 Synthesis of few-layer hexagonal boron nitride thin film by chemical Vapor deposition *Nano Lett.* **10** 4134–9
- [105] Hadid J *et al* 2022 Molecular beam epitaxial growth of multilayer 2D-boron nitride on Ni substrates from borazine and plasma-activated nitrogen *Nanotechnology* **34** 035601
- [106] Bisswanger T, Winter Z, Schmidt A, Volmer F, Watanabe K, Taniguchi T, Stampfer C and Beschoten B 2022 CVD bilayer graphene spin valves with 26  $\mu\text{m}$  spin diffusion length at room temperature *Nano Lett.* **22** 4949–55
- [107] Pálkás A *et al* 2022 The composition and structure of the ubiquitous hydrocarbon contamination on van der Waals materials *Nat. Commun.* **13** 6770
- [108] Ferrari A C *et al* 2006 Raman spectrum of graphene and graphene layers *Phys. Rev. Lett.* **97** 187401
- [109] Graf D, Molitor F, Ensslin K, Stampfer C, Jungen A, Hierold C and Wirtz L 2007 Spatially resolved raman spectroscopy of single- and few-layer graphene *Nano Lett.* **7** 238–42
- [110] Ferrari A C and Basko D M 2013 Raman spectroscopy as a versatile tool for studying the properties of graphene *Nat. Nanotechnol.* **8** 235–46
- [111] Forster F, Molina-Sanchez A, Engels S, Epping A, Watanabe K, Taniguchi T, Wirtz L and Stampfer C 2013 Dielectric screening of the Kohn anomaly of graphene on hexagonal boron nitride *Phys. Rev. B* **88** 085419
- [112] Sonntag J, Watanabe K, Taniguchi T, Beschoten B and Stampfer C 2023 Charge carrier density dependent Raman spectra of graphene encapsulated in hexagonal boron nitride *Phys. Rev. B* **107** 075420
- [113] Lin Y-C, Lu C-C, Yeh C-H, Jin C, Suenaga K and Chiu P-W 2012 Graphene annealing: how clean can it be? *Nano Lett.* **12** 414–9
- [114] Schwartz J, Chuang H-J, Rosenberger M R, Sivaram S V, McCreary K M, Jonker B T and Centrone A 2019 Chemical identification of interlayer contaminants within van der Waals heterostructures *ACS Appl. Mater. Interfaces* **11** 25578–85
- [115] Volmer F, Seidler I, Bisswanger T, Tu J-S, Schreiber L R, Stampfer C and Beschoten B 2021 How to solve problems in micro- and nanofabrication caused by the emission of electrons and charged metal atoms during e-beam evaporation *J. Appl. Phys.* **54** 225304
- [116] IEC TS 62607-6-6:2021(E) 2021 Nanomanufacturing—Key control characteristics—Part 6-6: “Graphene - Uniformity of strain in graphene analyzed by Raman spectroscopy
- [117] Ouaj Taoufiq *et al* 2024 Supporting data for “Benchmarking the integration of hexagonal boron nitride crystals and thin films into graphene-based van der Waals heterostructures” *Zenodo* (<https://doi.org/10.5281/zenodo.13684712>)